U.PORTO

FEUP FACULDADE DE ENGENHARIA
UNIVERSIDADE DO PORTO

Digital Image Correlation for Vibration Analysis

Catarina Duarte Barros Ferreira

Mestrado Integrado em Engenharia Mecânica

Supervisor at FEUP:
Prof. Mário Augusto Pires Vaz (Associate Professor)

Supervisor at Siemens Industry Software NV:
Eng. Davide Mastrodicasa (Researcher)

Porto, 2021

Abstract

One of the main points when dealing with mechanical products and structures design is the vibrations control. Hence, their dynamic behavior has to be very well known. Normally, to do that, vibration measurements and experimental modal analysis (EMA) are used.

A new procedure, that avoids the problems related to the point-wise transducers in contact with the test surfaces that are commonly used, relies on the digital image correlation (DIC) to estimate the modal parameters of the structure under analysis. Optical methods have been receiving the attention from the researchers because they allow to get full field measurements without direct contact with the surfaces and without the mass loading effect.

In this work, the possibility of using DIC to perform modal analysis and to validate and update finite element models (FEM) is investigated through several tests in different conditions. Different types of excitation and cameras and two different test objects are used. The results are then compared to the ones obtained with the conventional methods to understand the potential and weaknesses of the technique.

Keywords: Digital Image Correlation, Optical Techniques, Vibrations, Modal Analysis, Finite Element Model

Resumo

Um dos principais focos do projeto de componentes e estruturas em engenharia é o controlo de vibrações. Assim, o seu comportamento dinâmico tem que ser bem conhecido. Tipicamente isso é conseguido através de testes de vibrações e técnicas de análise modal experimental (AME).

Uma abordagem inovadora, que evita os problemas associados aos transdutores pontuais e de contacto que normalmente se usam, consiste na utilização da correlação digital de imagem (CDI) para estimar os parâmetros modais do objeto em estudo. Os métodos óticos têm sido alvo de grande interesse de investigação pois permitem medições em toda a superfície sem contacto direto com a estrutura e sem a adição de massa.

Neste trabalho, a possibilidade de utilizar CDI para análise modal e para a validação e atualização de modelos de elementos finitos (MEF) é investigada através de testes em diferentes condições. São utilizados diferentes tipos de excitação, diferentes tipos de câmaras para a aquisição das imagens e dois objetos de teste distintos. Os resultados são então comparados com os obtidos pela via convencional para se compreender as potencialidades e as limitações desta técnica.

Palavras-chave: Correlação Digital de Imagem, Métodos Óticos, Vibrações, Análise Modal, Modelo de Elementos Finitos

Para a Avó Cinda

Recomeça...
Se puderes
Sem angústia
E sem pressa.
E os passos que deres,
Nesse caminho duro
Do futuro
Dá-os em liberdade.
Enquanto não alcances
Não descanses.
De nenhum fruto queiras só metade.

E, nunca saciado,
Vai colhendo ilusões sucessivas no pomar.
Sempre a sonhar e vendo
O logro da aventura.
És homem, não te esqueças!
Só é tua a loucura
Onde, com lucidez, te reconheças...

Miguel Torga, Sísifo

Acknowledgements

The work here present is the result of the learning process and the experiences I have been through over many years and that would never been possible without the help of some people to whom I want to express my gratitude.

First, to Faculdade de Engenharia da Universidade do Porto, that during the last years saw me grow as a person and as a future engineer. There, I had some of the best experiences and some of the most challenging ones, all of them contributing for who I am today. Particularly to Professor Mário Vaz, who was my internal supervisor and guided this work.

Secondly, to Siemens Industry Software NV, in the person of my supervisor Eng. Davide Mastrodicasa who, being always available for helping me and following my work since day one, introduced me to the amazing world of research and provided this internship a great experience. Also to my Waterview family because nothing would be the same without them.

To all my family but in special to my grandparents, for everything they did for me, for all the love and for always being there, knowing exactly what I was in need. Without doubts they are my example in life. Hope to make you proud.

To Sofia, for everything we lived and for the daily challenge that was growing up together, trying to teach her all and ending up learning everything. It has been a pleasure to follow her journey and be part of it, being sure that the best things are still to come. Thanks for making me the proudest sister in the world.

To my parents, there are no words to express the feeling. For the unconditional support and comprehension, for never letting me give up and for turning the impossible into possible for me. For always trust my decisions even after the repeated mistakes. For being the first to encourage me to pursue my dreams and the first to got my back when things do not go as planned. For showing me, with their way of life, what strength and resilience are. I owe them everything I am, I lived and I achieved.

To all those who somehow doubted, thinking that this would never be possible for making me work even harder. Always remember: it is not about who goes faster but who goes further.

Contents

List of Figures

List of Tables

Chapter 1

Introduction

1.1 State of the Art

Vibration analysis is a key factor when talking about mechanical design. With the knowledge of the modal parameters of the system, it is possible to avoid the resonance frequencies problem during the operation, preventing fatigue and failure to occur before expected, and keeping it with the performance level required [1]. On the other side, the validation of complex mechanical products in a large range of applications such as automotive, aerospace, and other mechanical industries relies on experimental modal analysis.

At the state of the art, modal testing can be done with different measuring techniques. The classic approach consists of exciting the structure with an impact hammer or a shaker and measuring its response with accelerometers. However, this procedure presents some limitations regarding the instrumentation of the object under analysis. For large-size structures, a lot of sensors are needed to have a good characterization of its behavior. Also for very small structures it can be difficult to place the sensors in an accurate position. Moreover, it is unavoidable to have wires around the test object which can introduce undesired electrical noise to the signals acquired. Another problem related to the conventional transducers is that they have to be somehow attached to the structure, adding mass to it, and influencing the modal parameters. This is particularly relevant when testing lightweight objects like composite structures.

To overcome these problems, alternative optical methods have been studied across the last years [2; 3]. Non-destructive techniques such as the laser interferometry ones, Shearography [4] and Electronic Speckle Pattern Interferometry (ESPI) [5], are also used for vibration analysis [6]. Other options, that have recently been investigated because of their potential for Experimental and Operational Modal Analysis (EMA and OMA), are the Laser Doppler Vibrometer (LDV) and Digital Image Correlation (DIC). These two techniques are also compared to understand the advantages and the weaknesses of each one [7].

DIC is a non-contact technique that combines optical measurements with image processing and can be used to investigate the behavior of a structure, both in static and dynamic conditions [8]. It has been particularly relevant for structural analysis on aerospace and automotive fields and for rotating structures like wind turbines [9; 10] or helicopter rotor blades [11]. Some tests were also done to understand the possibility of applying it to specimens in motion such as rolling tires [12] or rotating beams [13]. Due to its full field capability, DIC has also been investigated as a technique to achieve more reliable FE model validation and update [3]. Several experiments have been performed with high speed cameras to measure high frequency vibration [14]. but also under-sampling and signal remapping techniques have been investigated to allow the use of cheap low speed cameras for this propose [15–17].

Because of being an optical technique, DIC only measures on surfaces that are visible from the camera point of view which means that the hidden surfaces of the specimen are not analysed. Some research has been done to investigate the possibility of combining DIC with point-wise sensors and compensate this question [18]. One of main problems regarding DIC at the state of the art are the measurements at high frequencies, where displacements are too small and lower than the camera noise, resulting in a very noisy data set. The use of accelerometers together with DIC can also be an option to identify natural modes at higher frequencies [19]. Other application for DIC that has been studied is in structural health monitoring and damage detection of lightweight structures [20; 21].

At the state of the art, the main concerns regarding DIC for vibrations analysis are the big amount of data generated and the noise floor of the cameras that limits the reachable bandwidth [22]. Sensitivity analysis on the speckle pattern quality has been done to improve the results [23; 24].

1.2 Motivation

Today's societies have become increasingly dependent on technology and adopt lifestyles that demand from industry and, therefore, from research and engineering to develop materials that meet their needs, in performance and resistance, and also with low production costs. Thus, the challenge for the scientific and technological community to develop these materials and test them is great, using increasingly effective methods of testing and analysis of results that ensure that the performance/cost commitment is not compromised. Moreover, during the last years, there was a growth on the interest for the composite products for the mechanical and aerospace industries. This led to an increase number of lightweight structures to be tested in different contexts and situations. Hence, the mass load effect has to be avoided as maximum as possible during the experiments. Those are the main motivations behind the research and development of the Digital Image Correlation as an option to perform vibration measurements and modal analysis.

1.3 Objectives

- Gain insight in the state-of-the-art DIC structural vibration analysis techniques and processing;
- Increase the knowledge on signal acquisition and signal processing;
- Perform Experimental Modal Analysis (EMA), with DIC and pointwise sensors, and use numerical modal analysis techniques;
- Perform test campaign or collection of experimental data for the application and development of DIC modal analysis processing;
- Development of a straight procedure for performing FE model validation and update using DIC data;
- Development of a smooth procedure for the state-of-the-art FE model validation and update;
- Gain skills on FE model validation and update using Finite Element Analysis software (Simcenter 3D).

1.4 Layout

This work is divided in 5 chapters. The second one covers all the theoretical background that is needed to support the correct understanding of the following ones. The third chapter describes the procedures adopted to test and process the acquired data, from the vibration analysis point of view, from the surface of a dryer machine, using high speed cameras. In the fourth chapter a scaled wind turbine blade is tested with low speed cameras in order to validate and update its finite element model. In the end, there is one chapter where the main conclusions regarding this thesis are summarized together with some suggestions for future work.

Chapter 2

Theoretical Background

2.1 Experimental Modal Analysis

Nowadays, structural vibration problems are one of the main concerns when talking about engineering design. This sets the importance of being able to anticipate the vibration levels that will be found in operation, in a way that allows engineers to control them. Hence, it is fundamental to have a deep knowledge of the dynamic behavior of every real system. Modal analysis is the technique that investigates the structure focusing on the estimation of its dynamic properties such as frequency, damping and mode shapes [1]. There are two different approaches to study the vibrations of a system. One option to perform modal analysis is the analytic way, solving analytically the equations that describe the dynamic of the system because they can be written in terms of mass, stiffness and damping matrices (known properties of the system). Other option is using models of the system that can be either Finite Element Models or Experimental Modal Models.

Measuring the dynamic input forces on a model that represents the system (or on the system itself) and their respective output responses allows to estimate the modal parameters. With these measurements one can calculate the ratio between the output and the input, in the frequency domain, and obtain the so called Frequency Response Function (FRF). Theory shows that these functions can be written in terms of natural frequency, damping ratio and mode shapes and this is the idea behind Experimental Modal Analysis [25]. The main theoretical concepts that are needed to understand how EMA works will be summarized along this section.

2.1.1 Basic Concepts on Modal Analysis

Almost all the real situations have to be modelled into systems with more than just one degree of freedom (DOF) but this section will start with the analysis of the Single Degree of Freedom systems (SDOF) because they are simpler. The conclusions will be later extended for Multiple Degree of Freedom (MDOF) systems, owing the fact that the modal

properties of this kind of system can be seen as a linear superposition of the properties for a certain number of SDOF systems.

2.1.1.1 Single Degree of Freedom Systems

The analysis of the free response of an oscillatory system, or in other words, the system behavior when there are no external forces applied, allows to determine its modal parameters that are, for a SDOF situation, the natural frequency ω_n and the damping ratio ξ.

A basic model for a viscously damped SDOF system composed by a mass m, a spring with stiffness k and a damper with a damping coefficient c is represented in figure 2.1. The displacement of the mass is represented by $x(t)$ and $f(t)$ is the external force applied to the system, both as function of the time.

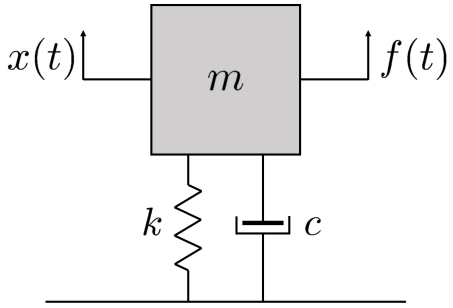

Figure 2.1: Single degree of freedom system.

For this case, the force equilibrium (balance between inertial, damping, elastic and external forces) is:

$$m\ddot{x}(t) + c\dot{x}(t) + kx(t) = f(t) \tag{2.1}$$

where $\dot{x}$ and $\ddot{x}$ are, respectively, the velocity and acceleration of the system.

Considering that there is no displacement neither velocity in the initial moment, i. e. $x(0) = 0$ and $\dot{x}(0) = 0$, and applying the Laplace Transform, the equation 2.1 can be written as:

$$(ms^2 + cs + k)X(s) = F(s) \tag{2.2}$$

Using Z as the dynamic stiffness of the system it comes:

$$Z(s)X(s) = F(s) \tag{2.3}$$

Replacing $Z(s)$ by $H(s) = Z^{-}1(s)$ the result is:

$$X(s) = H(s)F(s) \tag{2.4}$$

H(s) is known as the *transfer function* of the system and relates the force F (input)

to the displacement X (output). In general terms a transfer function of a system is a complex valued function and can be defined as the ratio of the Laplace Transform of the output (response of the system) to that of the input (excitation of the system), with zero initial conditions.

Going back to the equation 2.2 it is possible to rewrite the expression that defines *H(s)* in terms of the system dynamic properties (equation 2.5).

$$H(s) = \frac{\frac{1}{m}}{s^2 + \frac{c}{m}s + \frac{k}{m}} \tag{2.5}$$

The roots of the denominator of the equation 2.5, also called *system characteristic equation*, are the *system poles*. They are calculated by:

$$\lambda_{1,2} = -\frac{c}{2m} \pm \sqrt{\left(\frac{c}{2m}\right)^2 - \frac{k}{m}} \tag{2.6}$$

Considering that the system in analysis is conservative, i.e. it does not have damping ($c = 0$), the positive solution of the equation 2.6 is:

$$\omega_n = \sqrt{\frac{k}{m}} \tag{2.7}$$

where ω_n is the *undamped natural frequency* of the system, in radians per second (rad/s).

Equaling the term under the square root in the equation 2.6 to zero, one gets as solution the *critical damping* c_0:

$$c_0 = 2m\sqrt{\frac{k}{m}} \tag{2.8}$$

The damping of the system can also be defined in a dimensionless way, using the *damping ratio* ξ [26]. This represents the fraction of the critical damping that the system really has:

$$\xi = \frac{c}{c_0} \tag{2.9}$$

The damping ratio value determines the type of response that the system will have so it is used to classify them. A system with $\xi = 0$ has no damping. When the damping ratio is between 0 and 1, the system is called underdamped. If the damping coefficient is equal to the critical damping, $\xi = 1$ and it is classified as critically damped. When the damping ratio is higher than 1 the system is overdamped. Without any active damping mechanism, the real world systems are normally underdamped, with the damping ratio lower than ten percent ($\xi < 0.1$) in the most cases. Because of that, from now on, the systems in analysis are all consider as underdamped.

Recovering the equation of motion for the system (2.1) and solving it in the time domain:

$$x(t) = x_1 e^{\lambda_1 t} + x_2 e^{\lambda_2 t} \tag{2.10}$$

where λ_1 and λ_2 defined by the equation 2.6 represent a solution of the homogeneous equation.The solution of that equation are two complex conjugate roots:

$$\lambda_1 = \sigma_1 + j\omega_1 \quad \text{and} \quad \lambda_1^* = \sigma_1 - j\omega_1 \tag{2.11}$$

with σ_1 being the *damping factor* and ω_1 the *damped natural frequency*, often close to the *resonance frequency*.

Knowing this, the equation 2.5 for the transfer function can be written as:

$$H(s) = \frac{\frac{1}{m}}{(s-\lambda_1)(s-\lambda_1^*)} \tag{2.12}$$

According to the theory of the partial fraction expansion, it is also true that:

$$H(s) = \frac{A_1}{(s-\lambda_1)} + \frac{A_1^*}{(s-\lambda_1^*)} \quad \text{with} \quad A_1 = \frac{\frac{1}{m}}{j2\omega_1} \tag{2.13}$$

where A_1 and A_1^* are the *residues*.

All the concepts introduced before in the Laplace domain (variable s) can also be rearranged to the frequency domain. The *Frequency Response Function (FRF)* is the transfer function evaluated along the frequency axis $j\omega$ (when $\sigma = 0$):

$$H(s)|_{s=j\omega} = H(\omega) = \frac{A_1}{(j\omega-\lambda_1)} + \frac{A_1^*}{(j\omega-\lambda_1^*)} \tag{2.14}$$

For frequencies close to the resonance frequency ($\omega \cong \omega_1$) , it is possible to ignore the effect of the complex conjugate part and simplify the expression for the FRF (2.15).

$$H(\omega) = \frac{A_1}{(j\omega-\lambda_1)} \tag{2.15}$$

There are 3 different types of frequency response function, according to the physic quantity used to measure the system response [27]. The *receptance* is the function calculated in terms of the displacement relative to the input force. It is also called dynamic compliance. If the FRF is measured in terms of velocity relative to the force then it is referred as *mobility*. When using the acceleration to measure the response the FRF is called *accelerance* or inertance. The plot in figure 2.2 shows the typical behaviour of the FRF compliance near the resonance frequency both for the real and for the imaginary part.

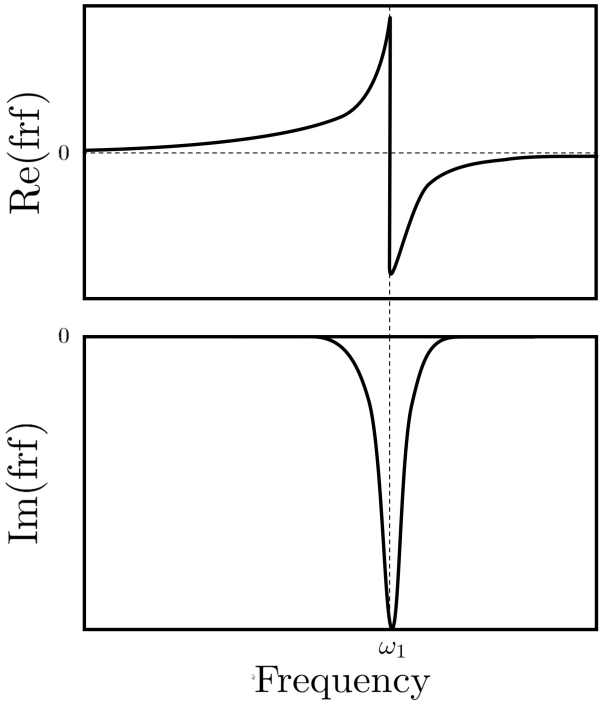

Figure 2.2: Receptance function - real and imaginary part.

2.1.1.2 Multiple Degree of Freedom Systems

Modeling problems with only one degree of freedom system is very restrictive and almost impossible for real life situations [1]. Therefore, the concepts introduced during the previous subsection will be extended to systems with n degrees of freedom, with $n > 1$.

The equation of motion of a MDOF system in the time domain has the same form as the equation of motion for a SDOF system but is a matrix equation:

$$[m]\{\ddot{x}\} + [c]\{\dot{x}\} + [k]\{x\} = \{f\} \tag{2.16}$$

where $[m]$ is the mass matrix, $[c]$ the damping matrix and $[k]$ the stifness matrix of the system. The dimensions of these matrices are n x n. The vectors $x(t)$, that represents the displacement as a function of the time, and $f(t)$, that is the excitation of the system also as a function of the time, have dimension n x 1 [25].

Assuming that the initial displacements and velocities are zero for all the degrees of freedom, the equation of motion can be transform into the Laplace domain and becomes:

$$([m]s^2 + [c]s + [k])\{X(s)\} = \{F(s)\} \tag{2.17}$$

or

$$[Z(s)]\{X(s)\} = \{F(s)\} \tag{2.18}$$

with $[Z(s)]$ being the dynamic stiffness matrix. The inversion of this equation results in:

$$\{X(s)\} = [H(s)]\{F(s)\} \tag{2.19}$$

where $[H(s)]$ is the *transfer function matrix* because represents the ratio between the response of the system and the respective force input in the Laplace domain for each DOF. This matrix contains complex valued functions.

The determinant of $[Z(s)]$ is the *system characteristic equation* and its roots are the *system poles* that define the values of the natural frequencies of the system. The solution of this problem is based on the eigenvalues of a matrix so the first step is to write the equation 2.17 in the general eigenvalue problem formulation. Considering:

$$[A] = \begin{bmatrix} [0] & [m] \\ [m] & [c] \end{bmatrix} \quad , \quad [B] = \begin{bmatrix} -[m] & [0] \\ [0] & [k] \end{bmatrix} \quad , \quad \{Y\} = \begin{bmatrix} s\{X\} \\ \{X\} \end{bmatrix} \quad \text{and} \quad \{F'\} = \begin{bmatrix} \{0\} \\ \{F\} \end{bmatrix}$$

and keeping in mind that

$$(s[m] - s[m])\{X\} = \{0\} \tag{2.20}$$

it comes:

$$(s[A] + [B])\{Y\} = \{F'\} \tag{2.21}$$

When the forcing vector is a null vector the equation 2.21 is the general formulation for the eigenvalue problem. The eigenvalues of the system (λ_r, with $r = 1, ..., n$) are the solutions of the following equation, solved in order to s.

$$\Big|s[A] + [B]\Big| = 0 \tag{2.22}$$

The number of solutions of this equation depends on the number of degrees of freedom that the system has, n. There are $2n$ complex valued eigenvalues and they appear in complex conjugate pairs. The real part of a pole is the damping factor, and the imaginary part is the damped natural frequency, just like in the SDOF systems.

There is an eigenvector associated to each eigenvalue of the system and it is called *mode shape vector*, $\{\psi\}_r$. They appear in complex conjugate pairs like the system poles. The modal vectors contain complex valued modal displacements and their phase can be different between elements. By definition, these vectors make the forcing vector null on equation 2.17. The transfer function can also be written in terms of the system poles since they are the roots of system characteristic equation:

$$[H(s)] = \frac{adj([Z(s)])}{\prod_{r=1}^{n} E(s-\lambda_r)(s-\lambda_r^*)} = \frac{adj([Z(s)])}{\prod_{r=1}^{2n} E(s-\lambda_r)} \tag{2.23}$$

where E is a constant.

As for the SDOF systems, the theory of partial fraction expansion can be applied to the previous expression and the *residues*, A_r can be obtained. They are related with the mode shape vectors by the following expression. For each residue:

$$[A]_r = Q_r\{\psi\}_r\{\psi\}_r^t \tag{2.24}$$

The residues $[A]_r$ are absolute quantities so, based on the equation above, it is possible to conclude that the modal vectors are scaled vectors depending on a scaling factor Q_r. Unless it is coincident with a modal coefficient ψ_{qr} equal to zero, each column q of the matrix $[A]$ has enough information to construct that matrix. This happens because all the columns are proportional to each other, but when the coefficient is zero, then the respective row and column will also be zero. As a consequence, in experimental modal analysis, if the excitation point is in a nodal point of one mode, that mode will not be detected.

Evaluating the transfer function matrix along the frequency axis one should obtain the frequency response function matrix:

$$[H(j\omega)] = \sum_{r=1}^{n}\left(\frac{Q_r\{\psi\}_r\{\psi\}_r^t}{(j\omega-\lambda_r)} + \frac{Q_r^*\{\psi\}_r^*\{\psi\}_r^{*t}}{(j\omega-\lambda_r^*)}\right) \tag{2.25}$$

The matrix $[H(j\omega)]$ has complex values and depends on the frequency of the input so its values are not constants. Remembering that the FRF is defined as the ratio between the output and the input, $H_{qk}(\omega)$ is the response X_q for the q DOF, when an excitation F_k is applied on the k DOF. Both the input force and the system response (whether it is in displacement, velocity or acceleration) are measurable quantities. Hence, the expression 2.25 allows to determine the modal parameters of the system using them.

As said before, the FRF of a multiple degree of freedom system is nothing else than the sum of the frequency response functions of n single degree of freedom systems.

2.1.2 Testing Procedures

Normally, when performing experimental modal analysis, and due to its practical aspect, it is not possible to measure the entire FRF matrix. During the tests, the number of modes detected is smaller than the number of points where the response is measured (number of outputs) which is also smaller than the number of degrees of freedom of the system [25].

To calculate the experimental FRFs, different types of inputs and outputs can be used. Normally, for testing mechanical systems, the inputs are in force and the outputs in acceleration, velocity or displacement. The input force can be applied to the structure and measured through an impact hammer or an electrodynamic shaker. The way to measure the response depends on the quantity of interest. If the objective is to measure the acceleration than the most obvious option is to use accelerometers. To measure the surface velocity a laser can be used. For the displacements the options include string pots

or digital image correlation, among others.

The force spectrum of the excitation provided to the test object should be flat versus frequency, meaning that the signal should excite all the frequencies with the same intensity. In this way, the peaks that appear in the response are at the natural frequencies of the system. When using the hammer to excite the object, this can be controlled with the correct selection of the tip. The FRFs are normalized to the input force because they are all calculated with the same reference. Hence, the peaks on this function are at the resonant frequencies of the structure under analysis.

To get better results for the modal parameters, it is common to calculate the FRFs several times and average them with the estimator method that suits better the objectives for the test. This ensures that the transfer function that is being measured is reliable. To check the repeatibility of each FRF, the coherence function is estimated because, indicating how much of the output is due to the input in the FRF, can be used as an indicator of the quality of the FRF. The value of the coherence varies between 0 and 1. When it is 0 or close to it the measurements are not repeatable and probably there is something wrong with the setup. From the other side, a coherence close to 1, indicates that both amplitude and phase of the FRF are repeatable.

The fact that the FRF is repeatable does not mean that the results will be the same. Structures are never one hundred per cent linear and for experimental procedures there are always external factors that influence the tests, like the instrumentation noise for example. Because of this, the results will never be exactly the same for the repeated measurements. This leads to the need of using estimators to calculate the average between the results and understand which one is more correct. The estimators are used to calculate the amplitude ratio (H) of the input to the output of FRFs. The most common ones are: H1, H2 and HV. The H1 considers that all the measurements of the excitation are accurate because there is no noise on the input, with all the noise being on the output of the system. The estimator H2 does the opposite, assuming that there is no noise on the output, only in the input. The HV estimator has into account noise both on the input and output and, despite requiring more computational effort, is better than the other two.

Having the FRFs for the structure, the following step is to calculate the natural frequencies and damping ratios. There are different techniques currently used to estimate the modal parameters of multiple degree of freedom systems such as Polyreference Least Squares Complex Exponential method (LSCE), Time Domain Direct Parameter Identification (TDPI), Ibrahim Time Domain method (ITD) or the Deterministic Subspace Identification in the Time Domain (DSSITD) for a time-domain analysis. Also for a frequency-domain analysis it is possible to use Non-linear Least Squares Frequency Domain method (LSFD), the Frequency Domain Direct Parameter Identification (FDPI) or the Complex Mode Indicator Function (CMIF) [25]. Along this thesis, the modal parameters estimation was always done using PolyMAX or PolyMAX Plus methods.

PolyMAX, or Polyreference Least Squares Complex Frequency Domain method, is a non-iterative frequency-domain parameter estimation method based on a weighted least-

squares approach [28]. First, the FRFs are used as primary data to obtain a stabilisation diagram containing frequency, damping and participation information. Then, after the selection of the stable poles by the user, the mode shapes are calculated in a second least squares step. This method retrieves a very stable identification of the system poles and participation factors as a function of the specified system order, which leads to stabilisation diagrams that are easy to interpret. One advantage of PolyMAX, comparing with the other methods available, is that the results are cleaner without an increase of the computational effort.

The PolyMAX Plus method was developed to improve the results of PolyMAX when the data set is noisy, adding some Maximum Likelihood Estimation (MLE) features [29]. It consists of 3 different stages being the first the statistically optimal MLE data smoothing. Secondly, PolyMAX mode selection is performed and finally, confidence bounds from MLE modal model are formulated. The method is optimized with respect to the computation time and memory requirements which allows to use more than 1000 FRFs. It estimates the modal parameters with great confidence even in very noisy cases.

2.2 Operational Modal Analysis

A different option for modal testing consists in measuring the response of the structure when it is operating, in order to find its modal parameters. This technique is called Operational Modal Analysis (OMA). In this case there is not any measured external input to excite the object so the method is also known as Output Only Modal Analysis. The main point of using OMA is that the object is tested in its real operation conditions, that sometimes are difficult to reproduce on the laboratory environment, making it more realistic. It can also be used to monitoring the condition of the structure in service for fatigue or damage detection and predict failure, avoiding the interruption of the operation for this measurements [30].

As well as for EMA, the goal of OMA is to build the mathematical model of the system´s dynamic characteristics and use it to determine its modal parameters. To extract them, a curve-fitting algorithm is applied. The model, based on functions in the frequency domain, establishes the relation between the inputs $[F]$ (excitation applied to the system) and the outputs $[X]$ (responses of the system to that excitation) in different points of the structure. These functions are called *auto-power spectra* and *cross-power spectra* and are rearranged into the *system transfer matrix*, $[H]$. The principal difference from OMA to EMA is the way used to define this matrix because in the operational tests the input forces are not measured. In EMA the input is known and measured so the procedures are developed in a deterministic framework however, when performing OMA, the input is not known neither measured so the procedures adopted are considered as stochastic [31]. Knowing only the output of the system during the test, the option behind OMA approach is consider that the input forces are random distributed in the space around the object and that it is of the form of white noise. This means that the input signal

has the same magnitude for all the frequencies in the bandwidth that will be analysed. With this assumption the responses of the system have all the information required to characterize the dynamic of the system, allowing to extract the modal parameters from the mathematical model created only with the measurement of the output. In this way there is no possibility for calculate the FRFs as it is done when performing EMA but it is still possible to extract the frequency information.

With the measured responses of the structure, the correlation functions are created. These are time domain functions that work as a statistical tool for finding repeating patterns in a signal, that can be hidden inside a signal that looks random. They can be use to compare a signal with itself in a delayed version at increasing time lags and, in that case, the functions are called *autocorrelation function* (ACF). This comparison retrieves a value between -1 and 1 according to the level of the correlation. When there is some periodic information inside the signal this value will be high at certain time lags. Increase the delay between the signals, should make the correlation values decrease until zero, assuming that the structure is being excited with a random signal. The ACF will retrieve the periodicities that are common between the signals compared and can be converted to the frequency domain. The cross-correlation function has the same principle as the ACF but instead of comparing the signal with a delay version of itself, makes the comparison with a reference signal. This function extracts the periodicities common between the response acquired in two different points [31].

To perform OMA one reference location is enough but it is also possible to select more measurement points as a reference. Then, with the measured response of the system in different points of the structure, auto correlation and cross-correlation functions are calculated and the common periods between the different measurements are extracted. This data is in the time domain so, making use of the discrete Fourier transform of the correlation functions, it is converted to the frequency-domain. The functions that result from this operation are called *correlograms* and show the dominant frequencies that are common across all the measurement locations. These functions are power spectra, i.e. a measure of the signal´s power content at each frequency, and the peaks can be determined applying the curve fit technique, just like in EMA.

2.3 Digital Image Correlation

Digital Image Correlation (DIC) is a measuring technique that can be used to obtain three-dimensional full field shape, displacement and strain of a surface, both in static or dynamic condition, under any arbitrary load [32]. It is an optical-numerical method since in one side optical sensors (such as cameras or microscopes) are used to acquire images of something deforming and in the other side there is a software platform where the images are loaded and processed. DIC works in a pattern tracking base so contrast in the surface is always needed. Natural contrast like the surface texture or the material micro structure can be used but the contrast can also be created with stickers, markers or spray paint for

example. This allows to track the position of the pixels across different pictures, the main goal of the correlation process. An example of this speckle pattern can be seen in figure 2.3.

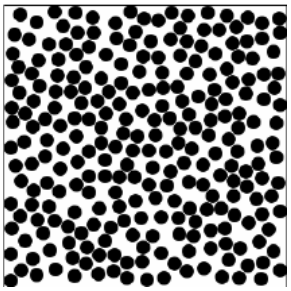

Figure 2.3: Example of a speckle pattern for DIC with black dots randomly spread on a white background.

When trying to locate a specific pixel in one image based on its grey level it is possible to find different matches because the pixel value is not a unique signature (the amount of grey levels available is always limited). To avoid that, instead of looking only for the pixel itself, the software normally looks to a window that also includes its neighborhood. That group of pixels is called *subset* or facet and has the required contrast to make the correspondence unique between the reference image and the deformed one. Due to the fact of introducing this local window, the final result, in the central point of it, will be the average displacement of the pattern within subset. To process the entire region of interest, a mesh composed by multiple subsets needs to be used. The size of the subset is an user defined setting but its lower limit depends on the quality of the pattern in the surface because the subset should include at least 3 features (or speckles). With a better pattern it is possible to use a smaller subset [32].

The upper limit of the subset size is connected to the spatial resolution pretended for the results. The largest the subset, the higher is the resolution so the results can be less accurate when comparing to the results obtained when using a smaller one. A good example of this is when there is a peak displacement, as shown in figure 2.4. The variance of the value inside each smaller subset is almost linear, which allows to describe the behaviour of the displacement along the peak (2.4a). When using a larger subset, the variance of the displacement within it has a higher order and the averaging process will result in displacement value that does not really match the measured one (3.2b).

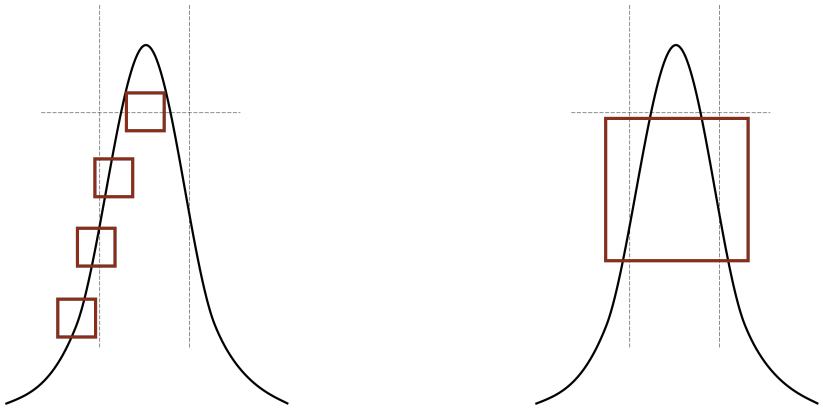

(a) Small subset. (b) Large subset.

Figure 2.4: Comparison between sampling with different subset sizes.

To choose the best subset size, one should keep in mind that oversized subsets can lead to problems matching the shape or deformation. In other hand, undersized subsets will not have enough speckle information.

Other important concept related to the mesh is the step size. Perform the correlation or, in other words, search for each pixel of the reference image in the deformed one, is not efficient from the computational point of view. So, instead of doing that, the software only retrieves the displacement for certain pixels. The distance between those displacement data points, measured in pixels, is called step size and can be defined by the user. With small steps the sampling is good but the computational effort may be too high. To reduce the computation time, bigger step sizes can be used but without forget that they can result in poor sampling and it comes with a loss in the accuracy of the correlation process. When using large steps, there are more points close to edges of the region of interest that are not correlated. The data point that is closer to the edge is, at least, half of the subset size away from it.

The three main components of the correlation process are the matching criterion, the interpolation function and the shape function. These concepts will be explained along the next subsections. An image is a matrix and each value represents, normally in a 8-bit or 16-bit format, the pixel value. This value is 0 when the point is black and is 255 (for the 8-bit format) when it is completely white. Hence, an image is a discretized representation of reality. The quality of the camera sensor will determine the level of that discretization.

2.3.1 Matching Criterion

During the correlation process, the software tries to guess where a certain point in the reference image is located in the deformed one, based on the grey levels within the subset. The goal is to find, among all the possible partners, the optimum point. It is the point in the deformed image that has the closest grey level to the data point in the reference image that is being correlated. This closest concept needs to be quantified and different methods can be used to define the correlation function.

Some common correlation criteria are [33]:

- Sum Squared Difference (SSD)
- Normalized Sum Squared Difference (NSSD)
- Zero Normalized Sum Squared Difference (ZNSSD)

Considering that F stands for the reference image grey values and G for the deformed image grey levels, when using SSD, the correlation function is:

$$\chi^2 = \sum_i (G_i - F_i)^2 \tag{2.26}$$

where χ is the function to minimize and i is the pixel in the subset.

The correlation coefficient is a percentage measure for the quality of the correlation and is given by $1 - \chi^2$. A correlation coefficient of 1 means that the correlation was fully successful while 0 means that the correlation is impossible.

Considering x and y the coordinates of the pixel in the reference image, the correlation function can also be written like

$$\chi^2 = \sum_i (G_i[\mu(x, y, \vec{s}), v(x, y, \vec{s})] - F_i(x, y))^2 \tag{2.27}$$

where $\vec{s}$ is the parameter vector that relates the coordinates in the reference image to coordinates in the deformed image.

Images have always different intensities during the same test, and those differences are even more accentuated in 3D because it requires 2 cameras and the light in one camera will never be the same as in the other camera.

SSD method does not compensate for these illumination differences so, if the image becomes darker or lighter during the test, the correlation will get poorer. NSSD is able to compensate for an offset in the image contrast. However, if there is a shift in the image, the software will not be able to compensate for that and it will result in lower values for the correlation coefficient as well. When using ZNSSD, the results are the same even if there is a shift or a difference of contrast between the images acquired during the test. This matching criterion compensates for the average grey values within the subset, according the following correlation function:

$$\chi^2 = \sum_i \left(\left(\frac{\sum \overline{F}_i \overline{G}_i}{\sum \overline{G}_i^2} G_i - \overline{G} \frac{\sum \overline{F}_i \overline{G}_i}{\sum \overline{G}_i^2} \right) - (F_i - \overline{F}) \right)^2 \tag{2.28}$$

Here, $\overline{F}$ and $\overline{G}$ represent those average grey values and can be define as

$$\overline{F} = \frac{\sum_i^n F_i}{n} \quad \text{and} \quad \overline{G} = \frac{\sum_i^n G_i}{n} \tag{2.29}$$

The function for the ZNSS method is more complex than the ones mentioned before so it comes with an extra cost in terms of computational effort, leading to a slower correlation process. The choose of the best matching criterion will relay in a balance between the accuracy of the process and the time it takes.

2.3.2 Interpolation Function

The true purpose of digital image correlation is to look at the subpixel level. As mentioned before, an image is a discretization of the reality and the goal is to recreate an image that looks more continuous. In this way it is possible to evaluate the grey levels values in between the pixels.

The interpolation process allows to do this because knowing the value for at least two different pixels, and applying the selected function, it is possible to calculate the grey value for a point between two pixels.

There are a lot of different interpolators but not all of them are good for each situation. The user can choose which one to use, considering that a good option should match the value at pixel locations, minimize the phase and the amplitude errors and provide filtering to the results.

2.3.3 Subset Shape Function

The subset changes its location between the reference image and the deformed one and also changes its shape. This means that the subset, that is a square in the reference image, does not remain a square in the deformed images. Because of that, the correlation process needs the flexibility to adjust the shape of the window according to the deformation. The level of freedom in this deformation is defined with the shape function selected for the process. For example, with a first order (affine) shape function for a square, the subset describes a linear varying displacement field and is allowed to translate, to rotate, to scale and to shear, according the deformation. Using higher order shape functions is useful to describe more complex deformation fields and is a good option to compensate oversized subsets.

$$\begin{bmatrix} \mu(x,y,\vec{s}) \\ \nu(x,y,\vec{s}) \end{bmatrix} = \begin{bmatrix} x \\ y \end{bmatrix} + \begin{bmatrix} u \\ v \end{bmatrix} + \begin{bmatrix} \frac{\partial u}{\partial x} & \frac{\partial u}{\partial y} \\ \frac{\partial v}{\partial x} & \frac{\partial v}{\partial y} \end{bmatrix} \begin{bmatrix} \Delta x \\ \Delta y \end{bmatrix} + \begin{bmatrix} \frac{\partial^2 u}{\partial x \partial y} \\ \frac{\partial^2 v}{\partial x \partial y} \end{bmatrix} \Delta x \Delta y + \begin{bmatrix} \frac{\partial^2 u}{\partial x^2} & \frac{\partial^2 u}{\partial y^2} \\ \frac{\partial^2 v}{\partial x^2} & \frac{\partial^2 u}{\partial y^2} \end{bmatrix} \begin{bmatrix} (\Delta x)^2 \\ (\Delta y)^2 \end{bmatrix} \quad (2.30)$$

Increasing the order of the shape function gives more flexibility to the correlation process but increases the number of unknowns it the mathematical expression. Hence, the computational effort associated to it is higher.

2.3.4 Camera Noise

When analyzing different pictures taken of a static object, all the features of the speckle should be exactly in the same place because there are no displacements on the surface. Hence, no variations in the grey level of each pixel between the different images are expected. In other words, subtracting the matrix of the grey level values for each pixel of two static images should result in a matrix of zeros. However, this is not what happens during the real tests. It is possible to notice that the grey value of the pixels change from the reference image to the deformed one even in a static situation. These alterations can be at low frequencies or high frequencies and are independent from one pixel to another. They are due to the camera noise so are always present [32].

The noise comes from the sensor inside the camera and depends both on the temperature and on the digitization level. Normally, a higher temperature of the camera means that there would be more changes in the grey level of the pixels between static images. In order to know the accuracy of the final results, the magnitude noise of the camera should be evaluated for every experiment. To do that, one should perform the correlation process between a certain number of truly static images. The result of subtracting two of them is a matrix of values that are not zero but that follow a Gaussian Distribution. The mean value of this distribution is close to zero and its standard deviation represents the DIC noise floor, also called resolution. If the signal to measure is lower than this value it is not distinguishable from the noise which means that the only significant measurements are the ones above it.

2.3.5 3D DIC Work Principle

While with only one camera the system is limited to measurements in two in-plane directions, with two or more cameras, in what is called a stereo system, there is the possibility of measure in three directions [34]. Each camera observes the surface of the specimen from a different direction so, performing a triangulation process, allows to retrieve the coordinates of the points in the space. The scheme of the work principle of 3D DIC is in figure 2.5.

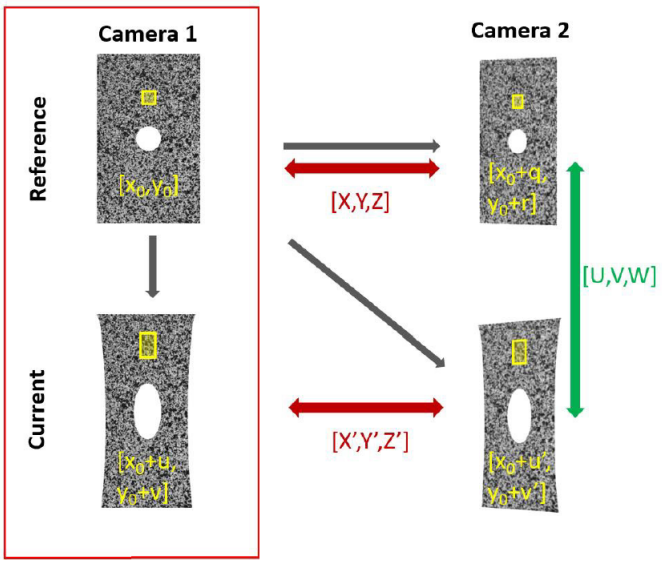

Figure 2.5: Work principle of stereo DIC [35].

The first image acquired for the camera 1 is used as reference and the first image acquired for the camera 2, at the same time, is compared to it. After performing the calibration process, the relative orientation of cameras is known so the corresponding points in the images from the two different cameras can be triangulated to the real position of the point in the space, represented in figure 2.5 by [X,Y,Z]. This process is repeated along the time to track the position of each one of the measurement points during the test. Hence, the correlation process retrieves all the deformation of the surface under analysis, denoted as [U,V,W] in the scheme.

2.3.6 Signal Reconstruction

To investigate the behavior of the structures at high frequencies with DIC it is needed to use high frame rates. However, when using high speed cameras, the increase of the sampling frequencies has as consequence the decrease of the frame resolution. To ensure good accuracy of the results, sometimes it is required to go above the Nyquist Shannon frequency limit for the maximum frame rate associated to the desired resolution. One possibility to measure vibrations at higher frequencies than the Nyquist frequency is based on the under sampling technique, where the excitation signal is replied several times. For this to be possible the signal has to be periodic. Then, low frame rates can be used together with a remapping process to reconstruct the signal [36]. In this way, triggering the camera at a very low frequency can retrieve the same results as if it was triggered at high frequency, despite taking more time to do it.

If the signal to be acquired (in blue in figure 2.6a) has a frequency f_{signal} and the sampling frequency used to measure it is f_{sample}, with $f_{sample} < f_{signal}$, then the reconstructed signal has a frequency f_r defined by:

$$f_r = f_{signal} \cdot f_{sample} \cdot (f_{sample}^{-1} - f_{signal}^{-1}) \tag{2.31}$$

The obtained signal S_r (in purple in figure 2.6b) has the same shape of the original one but it is scaled in terms of the time. Hence, the equation that describes it is:

$$S_r(t) = S_{signal}\left(\frac{f_r}{f_{signal}}t\right) \tag{2.32}$$

Knowing this, it is possible to reconstruct one period of the original signal and obtain the signal S_{artif} (represented in figure 2.6c), through the following expression:

$$S_{artif}(t) = S_r\left(\frac{f_{signal}}{f_r}t\right) \tag{2.33}$$

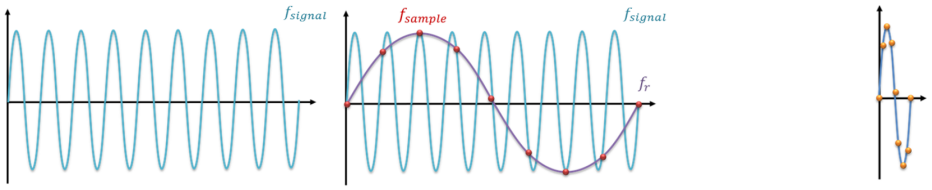

(a) Original signal. (b) Original and sampled signals. (c) Reconstructed signal.

Figure 2.6: Reconstruction process of a sine signal with frequency f_{signal} [18].

2.4 Finite Element Model Validation and Update

The finite element model of a structure is a very powerful tool to predict its behavior. However, it has to be validated otherwise is relying only on who did it or who is analysing it. Putting together the numerical model and the results of an experimental test creates a hybrid solution where the experimental mode set is used to validate the numerical results [37]. The first step of this approach is to create a correlation solution between the desired experimental mode set (the reference for the validation process) and the numerical ones.

The validation technique used by the software to perform the correlation is into one of the two categories:

- Modal based technique
- Frequency response based technique

With a modal based technique, the finite element model is changed to match its natural frequencies and mode shapes with the ones obtained with the test. One parameter that allows to evaluate the level of this correlation is the *Modal Assurance Criterion (MAC)*.

It is a scalar value that goes from 0 to 1 and is an indicator of the level of correlation between two mode shapes. If this value is close to 1 then the correlation is high, meaning that the mode shapes are similar and represent the same movement. If one mode shape is compared with itself then the MAC value should be 1.

To evaluate the MAC values for all the mode set, the MAC Matrix is plotted. It is nothing more than a matrix where each cell represents the value of the MAC between ψ_r and ψ_s, with r and s being the row and column respectively. In this way, one mode from one mode set is compared with all the modes on the other mode set.

The MAC is calculated as:

$$MAC(\{\psi_r\},\{\psi_s\}) = \frac{|\{\psi_r\}^{*t}\{\psi_s\}|^2}{(\{\psi_r\}^{*t}\{\psi_r\})(\{\psi_s\}^{*t}\{\psi_s\}} \tag{2.34}$$

Other option to compare the mode shapes consists on the *Coordinate Modal Assurance Criterion (COMAC)* [38]. It is an extension of the MAC that aims to identify which degrees-of-freedom have the main impact in a low MAC value. When to mode sets are compared, and the COMAC is calculated, there is a value for each degree-of-freedom measured.

The COMAC value is determined by the following expression:

$$COMAC_q = \frac{\sum_{r=1}^{L} |\psi_{qr}\phi_{qr}|^2}{\sum_{r=1}^{L} \psi_{qr}\psi_{qr}^* \sum_{r=1}^{L} \phi_{qr}\phi_{qr}^*} \tag{2.35}$$

where q is the degree of freedom considered [38].

With a frequency response based technique the correlation process is performed in order to match the FEM and the test model responses to a certain experimental excitation in the frequency domain. This means that the goal with this method is to match the FRFs of the two models.

Chapter 3

High Speed Cameras DIC on a Dryer Machine

3.1 Introduction

To explore the possibility of using DIC to perform Experimental Modal Analysis and Operation Modal Analysis and to study the accuracy of the results, different tests were performed. In order to find the natural frequencies, damping ratios and mode shapes of the structure, the FRFs were determined. From one side, the classical experimental analysis technique was applied and, based on the accelerometers measurements, the accelerance function was calculated for some points and used to estimate the modal parameters. On the other side, high speed cameras were used to grab pictures of the surface during the test. Then DIC technique was used to retrieve the displacements in the entire surface and, with those data, the receptance function was calculated for all the points. The modal parameters were extracted from them and the results compared with the other ones. The procedures adopted to perform those tests, the post-processing of the data acquired and the results obtained will be described on this chapter.

3.2 Experimental Modal Analysis

To perform experimental modal analysis on the dryer machine, and understand the feasibility of using high speed cameras to do it in different scenarios, two different types of excitation were used, resulting in two different tests. One of them was done with an impact hammer and in the other the input force was provided by an eletrodynamic shaker.

3.2.1 Experimental Setup

For all the tests covered on this section the dryer machine was on the floor, on its operational condition, and exclusively the lateral surface was analysed. For this reason, the experimental setup was almost the same in all of them, changing only the way to apply the excitation and the signals involved.

As explained in section 2.3, DIC requires a pattern with high contrast on the surface that will be under testing. Hence, the first step of the experimental process should be the object preparation. For the dryer machine surface, this contrast was created by attaching sticky paper with a printed random pattern to it. The pattern, consisting in black dots all with the same dimension and spread in a random way along a white background, was generated with the MatchID software. To have a reference to compare the DIC measurements with, the dryer surface was instrumented with five single axis accelerometers. The original specimen, a picture of the object preparation and the test version, are shown in figure 3.1. The figure 3.1c shows the test surface (the lateral one) all covered with the speckle pattern, where it is also possible to see the position of each one of the sensors, signalized with red squares.

(a) Original surface. (b) Speckling process. (c) Testing surface.

Figure 3.1: Preparation of the object for DIC tests.

The acquisition system used to record the input signals, i.e. the signal from the impact hammer and the one sent to the shaker, was the SCADAS from Siemens Industry Software NV. The response of the structure was measured with the accelerometers. The data from these sensors was also recorded through the SCADAS, as well as the signals used to trigger the cameras. The images were acquired with two iX Camera i-SPEED 513 high speed cameras, whose characteristics can be found in the table 3.1.

Table 3.1: iX Camera i-SPEED 513 specifications.

Parameters	**Values**
Resolution	1920 x 1080 pixel
Pixel Size	13.5 μm x 13.5 μm
Maximum Frame Rate at Full Resolution	6382 fps

A scheme of the full experimental setups, both for the test with the hammer and the test with the shaker, is present in the diagrams of figure 3.2.

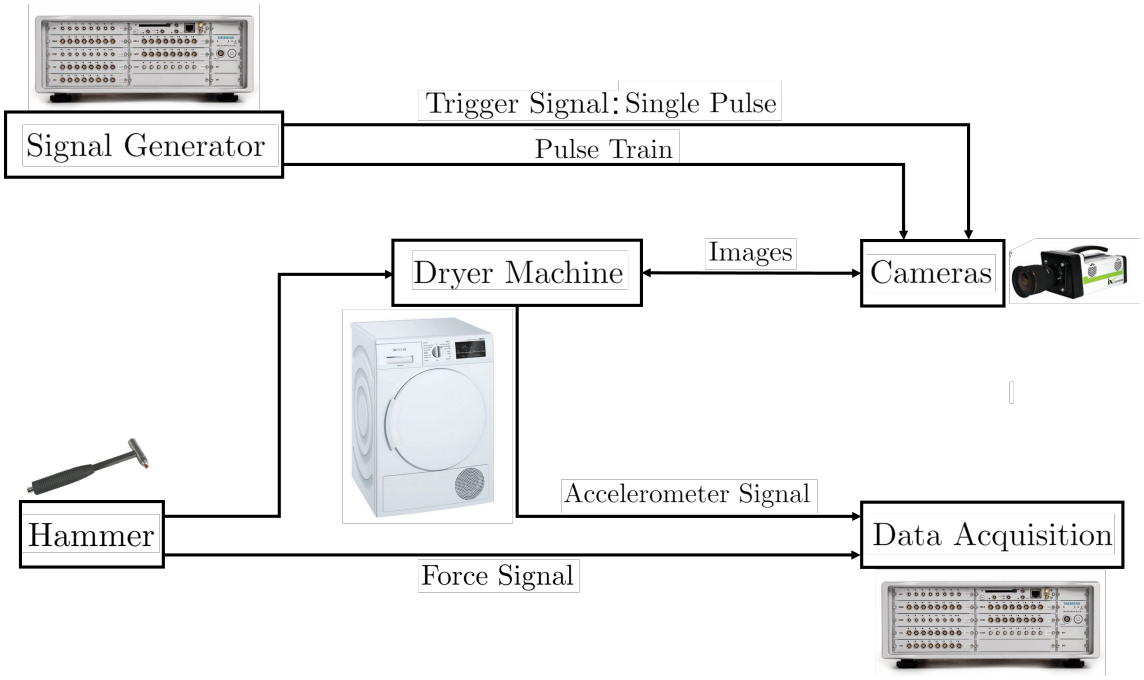

(a) Hammer test.

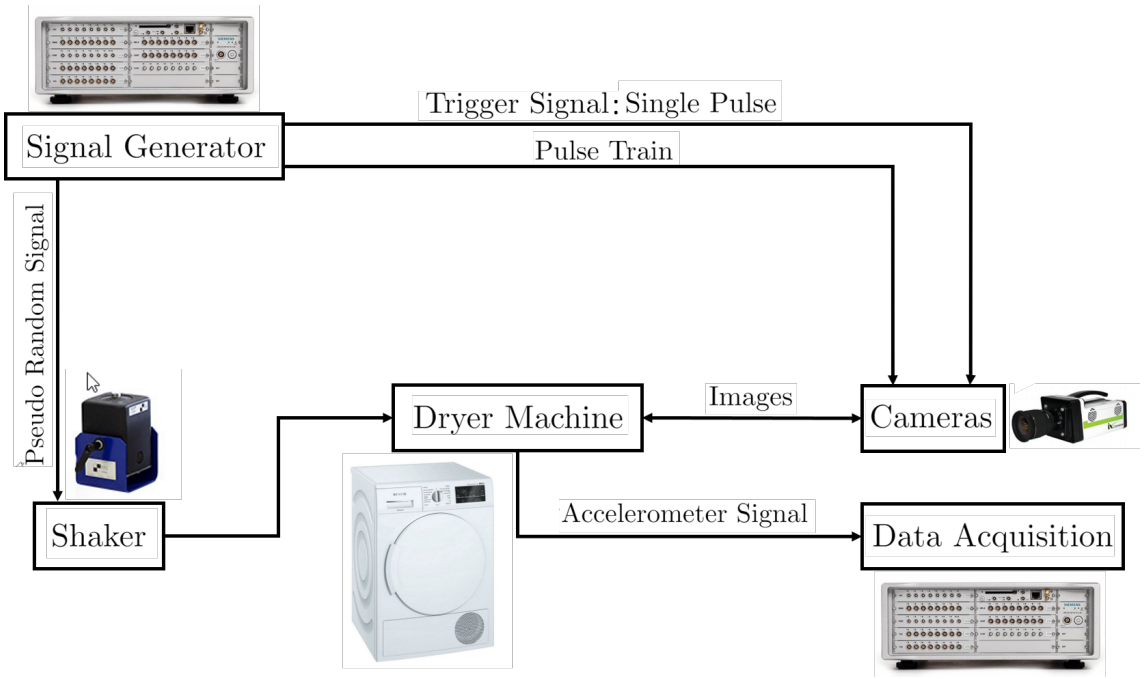

(b) Shaker test.

Figure 3.2: Diagram of full experimental setups.

The light during the test has to be strictly controlled so the white lights are other important part of the experimental setup. The DIC setup used, with the stereo system of cameras and the artificial lights, is shown in figure 3.3.

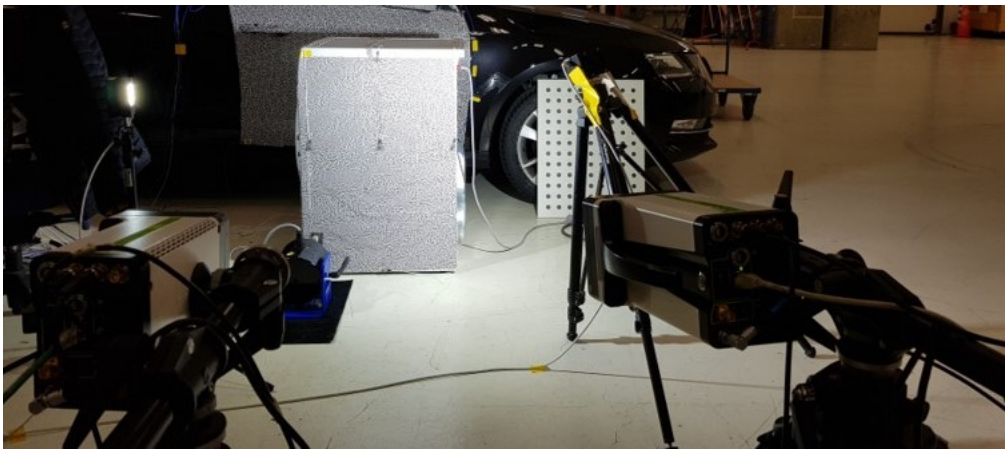

Figure 3.3: DIC experimental setup.

After the preparation of the experimental setup, and before every test, the light was adjusted, the cameras were correctly focused and the calibration of the stereo system was performed. This is needed to guarantee the right testing conditions and the accuracy of the measurements.

3.2.2 Hammer Test

The structure was excited with an ICP impact hammer model 086C03 from PCB, near the top left corner. The sampling frequency chosen for the signals was 800 Hz. According to Shannon´s Theorem, this means that the maximum frequency that can be acquired is 400 Hz [25]. The acquisition parameters are detailed in table 3.2.

Table 3.2: Acquisition parameters - hammer test.

Testlab Acquisition Parameters	
Parameters	*Value*
Bandwidth	400 Hz
Sampling frequency	800 Hz
Spectral Lines	512
Acquisition Time	1.28 s
MatchID Acquisition Parameters	
Parameters	*Value*
Sampling Frequency	800 Hz

The cameras start grabbing pictures when a button that is connected to SCADAS and whose signal is also recorded is pressed. They stop the acquisition when the internal memory is full. This means that the amount of pictures acquired during the test depends

on the storage available in the cameras, on their resolution and on the dimension of the pictures acquired. Because of this, when the specimen is smaller than the field of view, the image can be cropped to save memory. The time in which the cameras are recording depends on the number of images that will be stored and on the frame rate chosen for the images acquisition.

In the hammer test 10 impacts were done, so the final FRFs obtained are an average of the ratio between the output and the input for each impact. 12170 images were acquired and downloaded to the computer where they were processed with the Simcenter Digital Image Correlation software, in order to get the surface geometry and the full-field displacement time-history. Due to the high computational effort required for processing this kind of data, only the movement in the out of plane direction was studied. With the settings used for the correlation process, that can be seen in table 3.3, 5106 points were analysed. The geometry extracted from the DIC results is visible in figure 3.4. The white regions, without blue dots, are the points where the correlation was not succeeded or that were out of the region of interest selected, particularly near the accelerometers and its cables that were covering the speckle.

Table 3.3: DIC parameters - hammer test.

Parameters	**Values**
Subset Size	17
Step Size	16
Interpolation Function	Bicubic Splines
Shape Function	Affine
Matching Criterion	ZNSSD

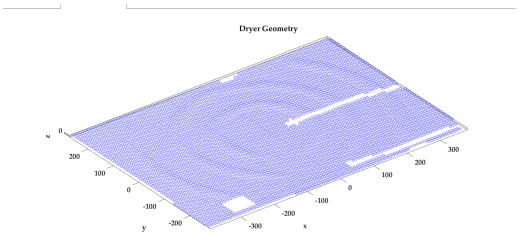

Figure 3.4: Dryer machine geometry.

The cameras do not start taking pictures at the same time that the SCADAS starts recording the signals, but only later, when a button is pressed. Hence, the first picture is not related to the point with $t = 0$ in the hammer signal. Because of this delay, a pre-processing step is required, in order to align the signals, before the FRFs calculation. The trigger is a 5 Volt signal sent to the cameras that drops to 0 Volt at the instant in which they should start the acquisition. That point was then considered as the new zero instant for the measurements so all the data acquired before it was deleted from the hammer signal. After, the displacement time-history for all the points considered was imported in Testlab. Using the recorded signal from the impact hammer as input force, the FRFs were calculated. The Impact Post Processing Tool was used to do this and only 9 impacts were analysed for the average processing. The last impact was discarded because the full response cycle related to it was not acquired with the cameras. The FRFs based on the accelerometers measurements were also calculated, considering the acceleration at

each corner and in the center as the system response to the excitation. Both for DIC and accelerometers data, H1 was used as estimator for the FRFs.

3.2.2.1 Accelerometers Results

To analyse the FRFs obtained with the accelerometers measurement the PolyMAX tool of Siemens Simcenter Testlab software was used. The sum of those five FRFs can be seen, as well as the Mode Indicator Function (MIF) and the possible modes, in the stabilization diagram in figure 3.5. In that figure, as well as in all the stabilization diagrams presented in this work, the sum of the FRFs is the line in red and the MIF is the line in green.

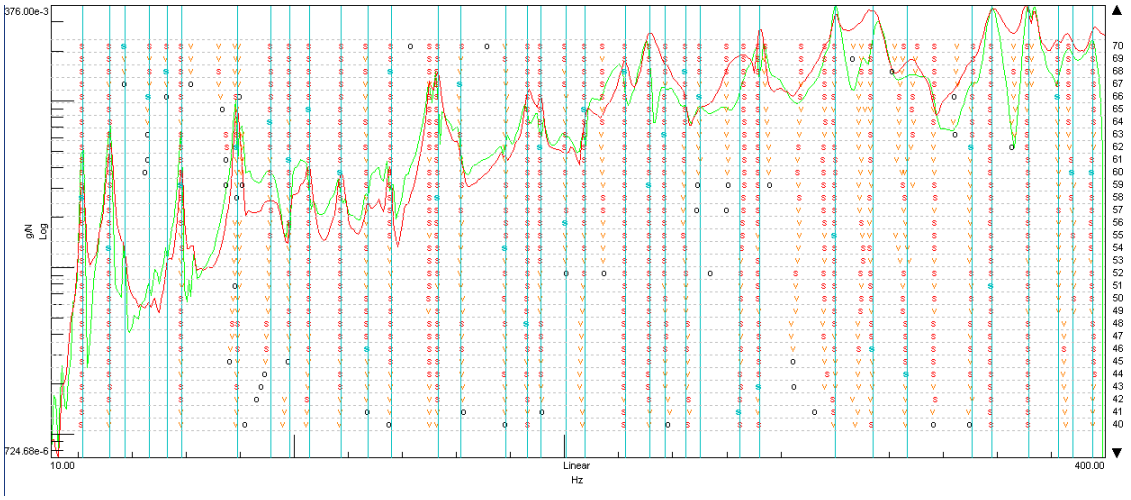

Figure 3.5: Stabilization diagram from accelerometers data.

In the bandwidth of interest (between 0 and 400 Hz), with PolyMAX algorithm and using a model order of 70, 36 natural modes of vibration were found and their respective mode shapes calculated. The first one was at 21.587 Hz with a damping ratio of 3.138% and the last one at 395.369 Hz with a damping ratio of 1.030%. The detailed results, in terms of natural frequencies and mode shapes can be seen on Appendix A.

For the mode set obtained with the accelerometers data acquired during the hammer test, the Auto-MAC was calculated and can be seen in figure 3.6. Red stands for 100% of correlation, meaning that the modes compared are exactly the same and dark blue stands for 0% of correlation.

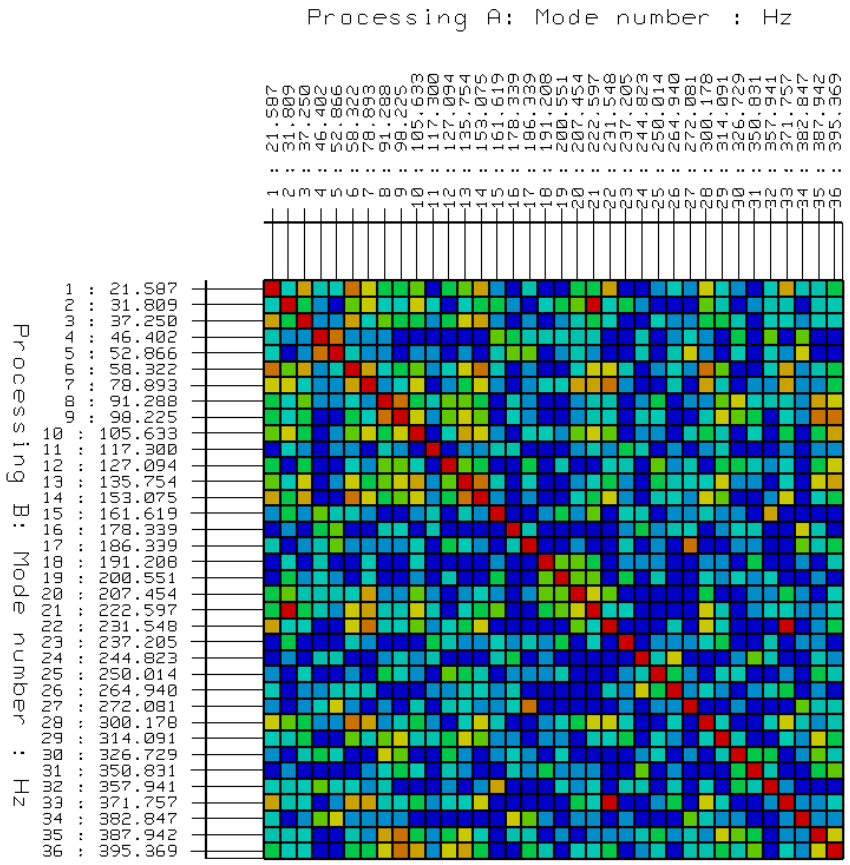

Figure 3.6: Auto-MAC for the mode set obtained during the hammer test with accelerometers

There are some high correlation values not expected outside the diagonal. This happens because five accelerometers are not enough to have the complete representation of the real natural mode of vibration and it is possible that the modes number 2 and number 21, for example, are the same on those points but different in all the others that do not have sensors.

3.2.2.2 DIC Results

When the vibration frequency gets higher, the displacements get lower, making it more difficult to measure with DIC. Hence, the signal starts to get noisier with the increase of the excitation frequency. Sometimes the values to measure are even below the noise floor of the cameras which means that they are not measurable with the chosen setup. Because of being a particularly noisy data set, the FRFs obtained from the DIC displacements were processed with the PolyMAX Plus tool. PolyMAX Plus allows to get better results, or at least detects more potential modes specially at high frequencies than PolyMAX, for the same model order, although the computation effort is much higher. The sum of the obtained FRFs, together with the MIF function and the stable poles found and selected is shown in figure 3.7.

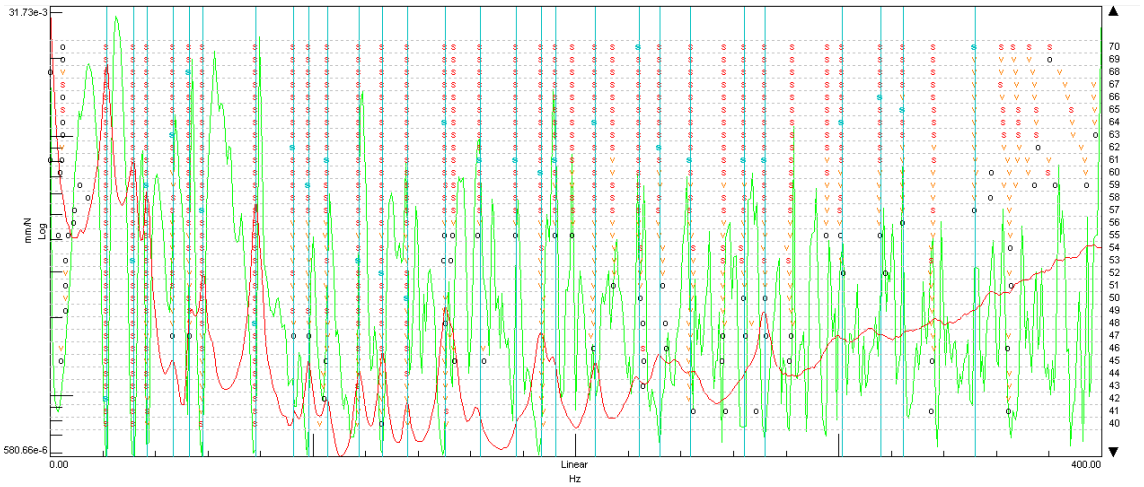

Figure 3.7: Stabilization diagram from DIC data.

Up to 400 Hz, 28 natural modes were selected and their mode shapes calculated with PolyMAX Plus (model order of 70). The first natural frequency found with the DIC data was 21.586 Hz and this mode have a damping ratio of 2.562%. The last natural mode detected was at 351.927 Hz with a damping ratio of 0.030%. All the natural frequencies and damping ratios of modes found with DIC for the hammer test can be found in appendix A. The auto-MAC for the mode set obtained, with the same color scale as the one for the accelerometers result, is in figure 3.8.

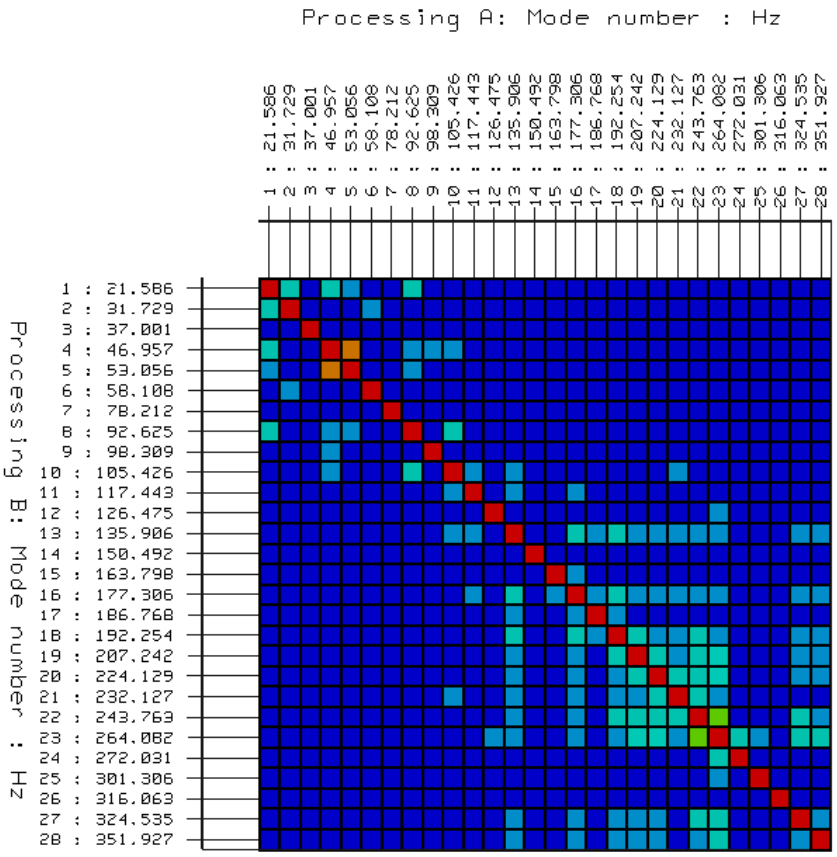

Figure 3.8: Auto-MAC for the mode set obtained during the hammer test with DIC

It is possible to see on the auto-MAC that the value of the correlation out of the diagonal increases a bit with the frequency, due to the effect of the noise in the measurements. The modes at high frequency are not so understandable, looking like the same in a big amount of points. Some of the modes calculated with the data set for the hammer test with DIC are in figure 3.9 where this behaviour is clear.

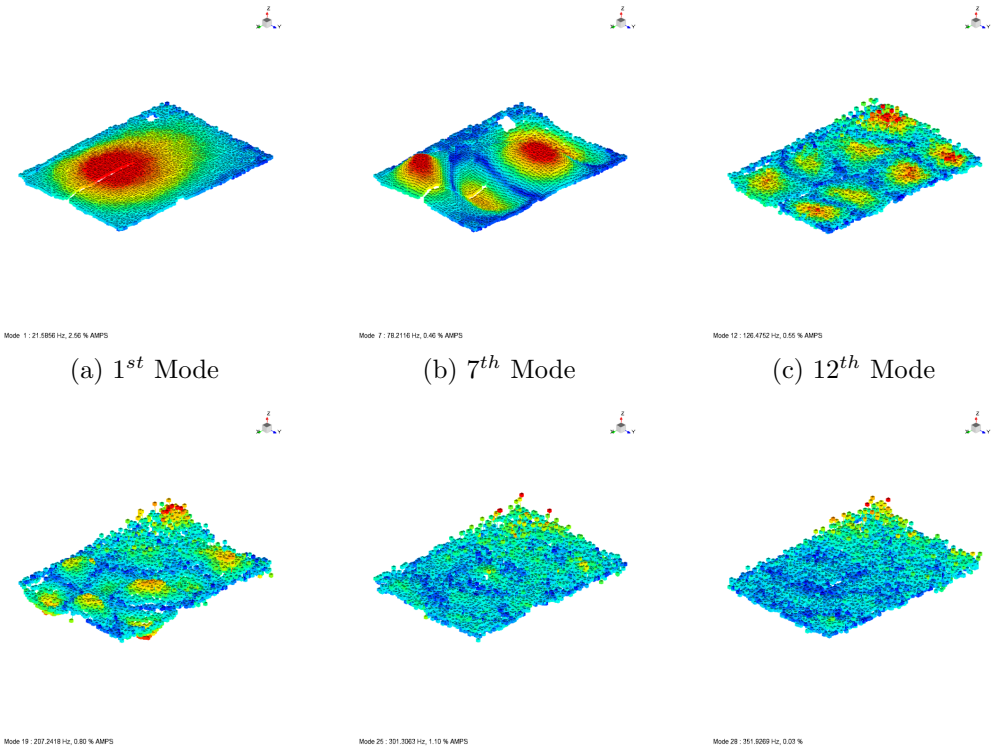

(a) 1^{st} Mode (b) 7^{th} Mode (c) 12^{th} Mode

(d) 19^{th} Mode (e) 25^{th} Mode (f) 28^{th} Mode

Figure 3.9: Mode shapes obtained for the hammer test with DIC.

3.2.3 Shaker Test

For this test, a pseudorandom signal was generated with SCADAS and sent to a PCB Shaker Model K2007E01, with an integrated power amplifier that allows to adjust the amplitude of the incoming signal. The shaker is connected to a load cell glued to the structure, also connected to SCADAS, acquiring the force that is being applied. This signal is used as the reference force for the FRFs calculation. The frequency of the periodic signal was varying between 10 Hz and 500 Hz. The load cell works also as an accelerometer so it is possible to have the response on the driving point. The sampling frequency, both for SCADAS and for the cameras was settled for 1600 Hz, meaning that it is possible to measure vibration up to 800 Hz. However, due to the fact that the structure was only excited between 10 Hz and 500 Hz, this will be considered as the bandwidth of interest for the FRFs calculation and analysis. All the acquisition parameters can be seen in table 3.4.

Table 3.4: Acquisition parameters - shaker test.

Input specification	
Parameters	*Value*
Signal Type	Pseudorandom
Bandwidth	10-500 Hz
Amplitude	6 V
Testlab Acquisition Parameters	
Parameters	*Value*
Bandwidth	800 Hz
Sampling frequency	1600 Hz
Spectral Lines	1024
Acquisition Time	1.28 s
DIC Acquisition Parameters	
Parameters	*Value*
Sampling Frequency	800 Hz

The cameras are triggered with a pulse signal generated in SCADAS that is aligned with the pseudorandom signal sent to the shaker. The peak of the pulse signal is in the beginning of the sixth period of the input to avoid the transient state of the system. During the test the cameras acquired 12170 images of the structure that were processed with Simcenter Digital Image Correlation software, retrieving the dryer surface geometry (figure 3.10) and the full field displacements time-history. The details of the correlation process are in table 3.5. Like in the hammer test, and because of the same reason, only the out of plane direction was considered during the analysis.

Table 3.5: DIC parameters - shaker test.

Parameters	**Values**
Subset Size	17
Step Size	16
Interpolation Function	Bicubic Splines
Shape Function	Affine
Matching Criterion	ZNSSD

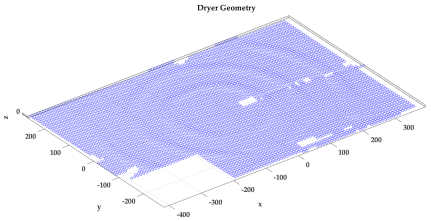

Figure 3.10: Dryer machine geometry.

The lack of correlated points in the corner, when comparing to the geometry obtained with DIC during the hammer test (figure 3.4), is due to the shaker positioning that covers that part of the dryer surface from the cameras point of view. This is visible in the experimental setup picture in figure 3.3. The obtained displacements were then imported in Matlab, together with the signal from the force cell, and used as the structure response

to calculate the FRFs for all the 4890 points correlated. To have the right alignment of the input and output signals, all the data points in the pseudorandom signal before the peak of the pulse signal were deleted. In this way the first image acquired matches in time with the first data point for the input signal. The FRFs based on the accelerometers measurements were calculated in Testlab with the data acquired with SCADAS. Both for DIC and accelerometers data, H1 was used as estimator for the FRFs.

3.2.3.1 Accelerometers Results

Using PolyMAX tool with a model order of 40, the sum of the FRFs obtained with the accerolmeters data was calculated and analysed. The resulting stabilization diagram is in figure 3.11.

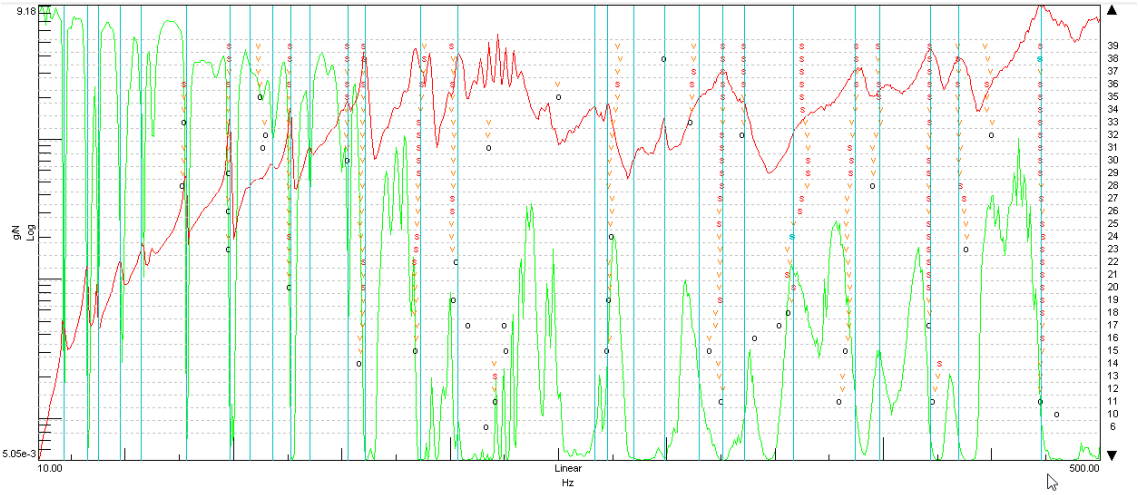

Figure 3.11: Stabilization diagram from accelerometers data.

Between 10 Hz and 500 Hz (the bandwidth of the excitation), 28 natural modes were found. The first at 21.899 Hz with a damping ratio of 2.098% and the last at 472.811 with a damping ratio of 1.584%. All the modal parameters found are detailed in appendix A. The mode shapes were also calculated and the autoMAC for this mode set was plotted. It can be seen in figure 3.12.

The effect of the reduced number of accelerometers on the dryer machine surface mentioned for the auto-MAC obtained for the hammer test is even more visible for this data set. Almost all the modes look the same, from the accelerometers point of view, due to insufficient sampling of the data along the surface. This is called the spatial aliasing effect.

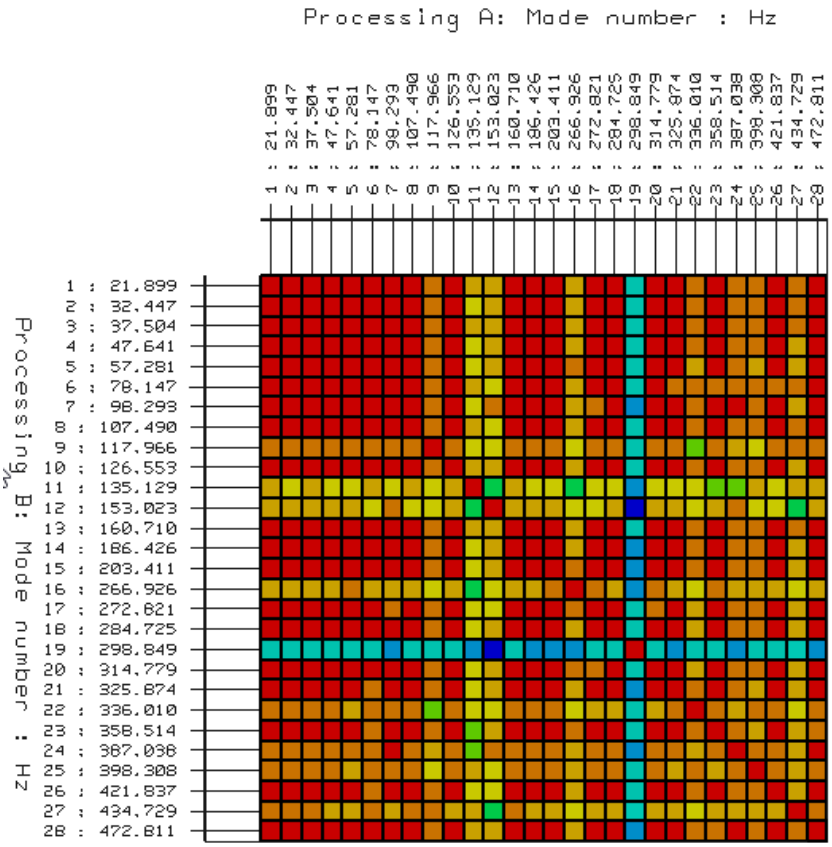

Figure 3.12: Auto-MAC for the mode set obtained during the shaker test with accelerometers.

3.2.3.2 DIC Results

The sum function of all the FRFs obtained with the DIC data was calculated and process with PolyMAX Plus in order to get the possible natural modes. The stabilization diagram obtained with a model order of 160 and the natural modes selected can be seen in figure 3.13.

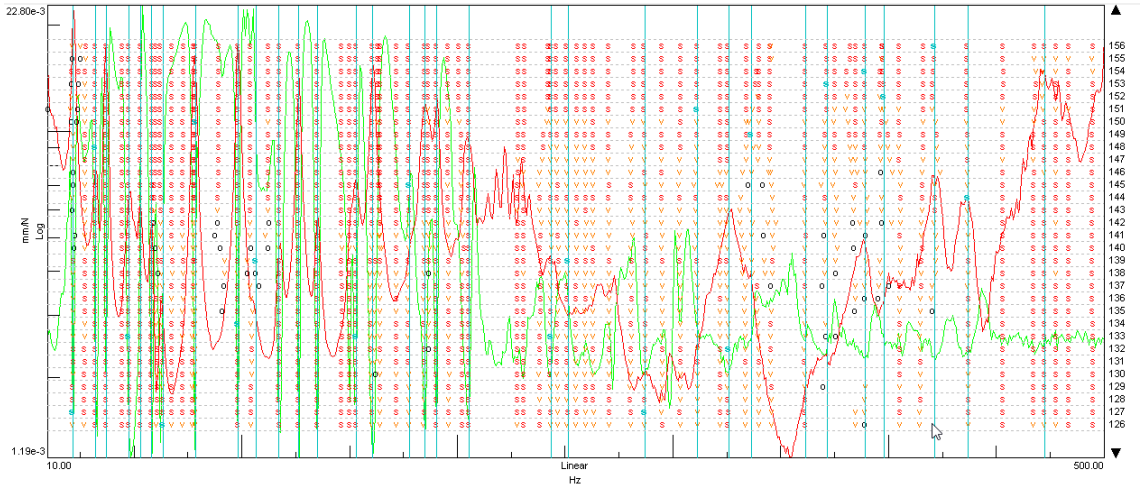

Figure 3.13: Stabilization diagram from DIC data.

In the bandwidth of interest 32 natural modes were found and their modes shapes calculated, starting with the first mode at 21.878 Hz with a damping ratio of 2.201% and the last one identified at 472.583 Hz with a damping ratio of 0.232%. The natural frequencies and damping ratio for the entire mode set are in tables on appendix A. For this mode set, the auto-MAC is the one in figure 3.14.

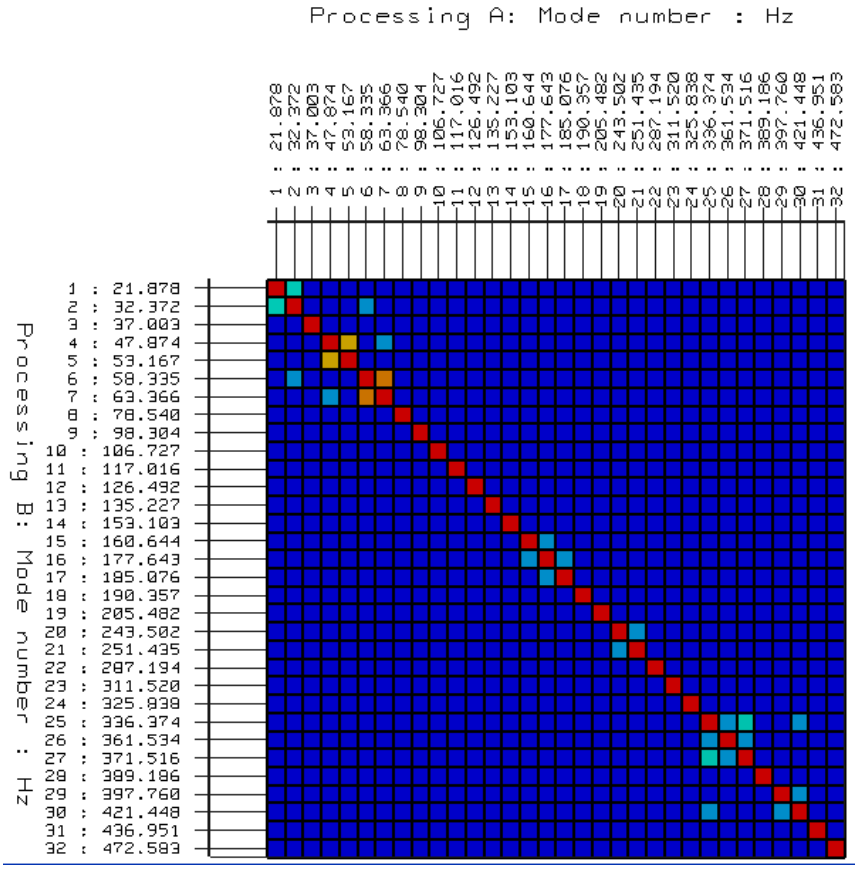

Figure 3.14: Auto-MAC for the mode set obtained during the shaker test with DIC

Modes number 6 and 7 have a high level of correlation, meaning that they are very similar, but they have two clearly different peaks in the stabilization diagram (3.13). However the peak around 63 Hz is only evident for this test and in specific with the displacement measurement (DIC data). Looking at these two mode shapes in figure 3.15 and 3.16 it is possible to understand that they have the same shape but it is more evident in mode 6. Despite the peak, that could be there because of external factors such as the boundary conditions or the coupling effect of the shaker, the 7^{th} peak selected is not a natural mode for the structure.

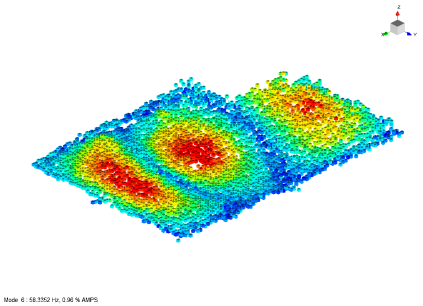

Figure 3.15: 6^{th} mode.

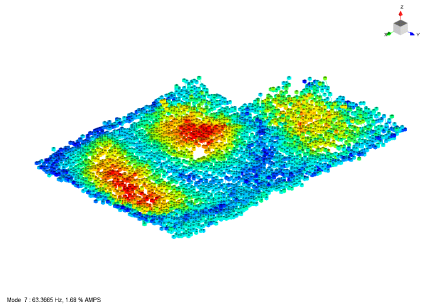

Figure 3.16: 7^{th} mode.

3.3 Operational Modal Analysis

During the third test performed on the dryer machine, it was running with one shoe, to have a bit of operational vibration inside. There was not any external excitation, in order to simulate the real working conditions. The experimental setup, in terms of acquisition systems and positioning of the object was the same as in the previous ones. To find the natural modes of vibration, an operational modal analysis algorithm was used. However, it was done in two different ways. One, with the response of the dryer machine measured as acceleration in five points, with the accelerometers displaced along the surface and whose signal was recorded with SCADAS, with a sampling frequency of 1600 Hz. The other method was measuring the displacement of all the points in the surface with DIC, and use it as the system response. The cameras were triggered as in the hammer test, with a button, and its sampling frequency was 1600 Hz. During the test they acquired 12170 pictures that were correlated with the parameters shown in table 3.6 and the geometry in figure 3.17 was obtained.

Table 3.6: DIC parameters.

Parameters	Values
Subset Size	17
Step Size	15
Interpolation Function	Bicubic Splines
Shape Function	Affine
Matching Criterion	ZNSSD

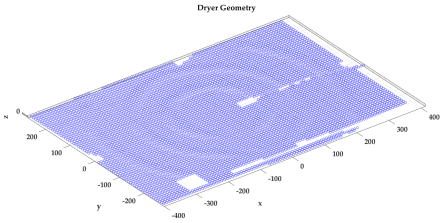

Figure 3.17: Dryer machine geometry.

Simcenter Digital Image Correlation software was used to calculate the displacements of all the points correlated and those time histories were processed in Siemens Simcenter Testlab, with the Operational Modal Analysis Tool. The auto and crosspowers were calculate in respect to 4 reference points, near the corners of the dryer machine surface under analysis. The auto and crosspowers with the accelerometers data were also calculated in Testlab.

3.3.1 Accelerometers Results

The set of crosspowers obtained with the accelerometers data was process with Operational PolyMAX, with a model order of 140. The obtained stabilization diagram, together with the selected poles, is in figure 3.18.

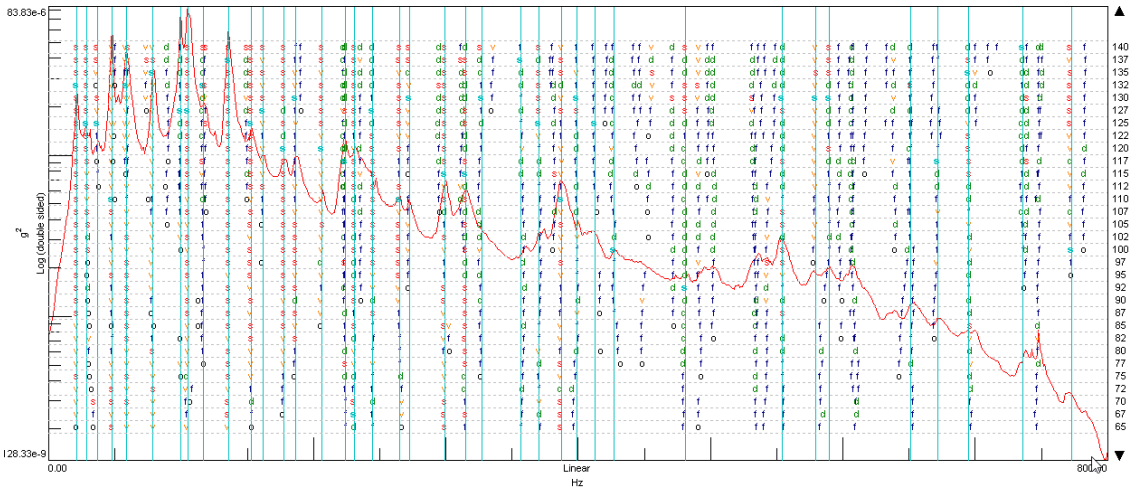

Figure 3.18: Stabilization diagram from accelerometers data.

The choosen sampling frequency allows to measure vibration between 0 and 800Hz and, in this range, 38 natural modes were identified. The first one has a natural frequency of 21.35 Hz and a damping ratio of 3.39 %. The last one was found at 772.8 Hz, with a damping ratio of 0.25 %. The other modes obtained are detailed in appendix A.

3.3.2 DIC Results

Operational PolyMAX Tool was used to analyse the set of crosspowers from the DIC data. The stabilization diagram obtained with a model order of 100 is in figure 3.19.

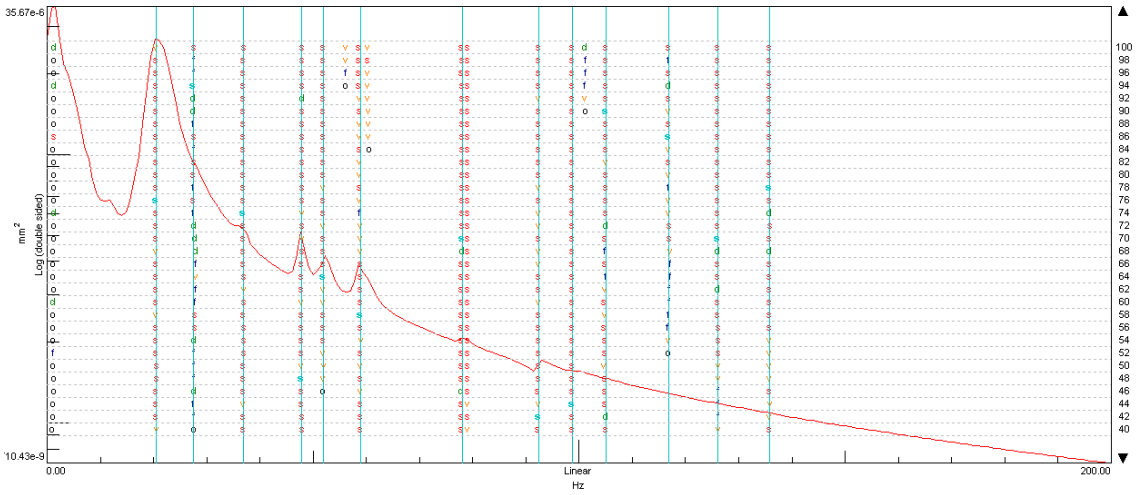

Figure 3.19: Stabilization diagram from DIC data.

In the bandwidth of interest 13 modes were found. The first at 20.48 Hz with a damping ratio of 3.81 % and the last one at 135.87 Hz with a damping ratio of 0.56 %. With Operational PolyMAX, and because DIC data are very noisy, it is not possible to identify modes in the entire bandwidth processed, as visible on the stabilization diagram. However, due to the very high computational cost of Operational PolyMAX Plus when selecting 4 reference points, it was not possible to use it. Some of the mode shapes calculated are in figure 3.20.

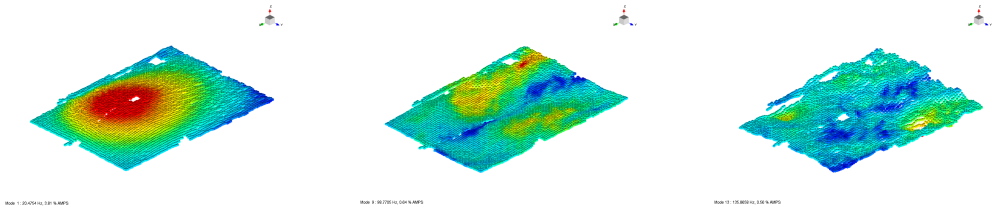

(a) 1^{st} Mode (b) 9^{th} Mode (c) 13^{th} Mode

Figure 3.20: Mode shapes obtained with OMA with DIC data.

It is possible to notice that the modes obtained with OMA are not so clear as the ones obtained when performing EMA, whether using the hammer or the shaker to provide the input force. This is due to the lack of measurements and also control regarding the excitation when performing OMA.

3.4 Comparison Between Accelerometers and DIC Results

To make a quantitative comparison between the natural frequencies and damping ratios obtained with DIC and the reference values obtained with the accelerometers, the relative error was calculated for each mode. This comparison is visible on tables in appendix A.

From the natural frequencies point of view the DIC results are very accurate. Comparing the values obtained with the ones calculated with the accelerometers data it is possible to see that the error is very low, never being higher than 2 % on the hammer and shaker tests mode sets. The maximum error in the results obtained with operational modal analysis is 4.94 % which is also a good indicative of the accuracy of the technique for determinate this parameter. The average relative error for the natural frequencies is 0.51 % with the hammer, 0.47% with the shaker and 1.37% for the OMA.

For the damping ratios the error varies a lot but in general has values that are too high. This probably happens because a good estimation of the damping ratios requires a lot of averages of the FRFs. Due to the limited space available to storage the acquired images this is not possible with DIC. However, this behaviour is still under investigation in order to work around the problem and improve the results.

Other difference between the results with accelerometers and DIC is the reachable bandwidth, because accelerometers have a better performance than DIC at high frequencies. For the hammer test it was possible to find the last mode at 395.37 Hz with the accelerometers and, if it was not because of the sampling frequency, it would be possible to go even higher. On other side, the last mode identified with DIC was at 351.93 and its mode shape is very noisy, making it difficult to understand the shape. For the shaker test, exciting the structure up to 500 Hz, the accelerometers data retrieve modes until 472.81 Hz. Almost the same value was reached with the DIC, with the last mode detected at 472.58 Hz. However, once again, the last modes calculated with DIC are not clean enough to correctly understand the shape. With operational modal analysis there is the biggest difference regarding the reachable bandwidth. The last mode found with accelerometers data was at 772.8 Hz while the last one with DIC was at 135.87 Hz.

The auto-MAC plotted for the mode sets should also be compared because they show a big difference between the two techniques used. The MAC values out of the diagonal, i. e. the correlation level between two different modes in the mode set selected, are much lower on the DIC data set. This is one of the advantages of having full field displacements and FRFs.

In terms of the FRFs obtained, the plots in figure 3.21 shows the comparison between the sum of the FRFs calculated with accelerometers and the ones obtained with DIC, both for the hammer test and the shaker test. To make the direct comparison easier, the FRFs sum obtained with DIC, that has unities of mm/N was double differentiated to be presented with unities of g/N as the FRFs obtained with the acceleration response.

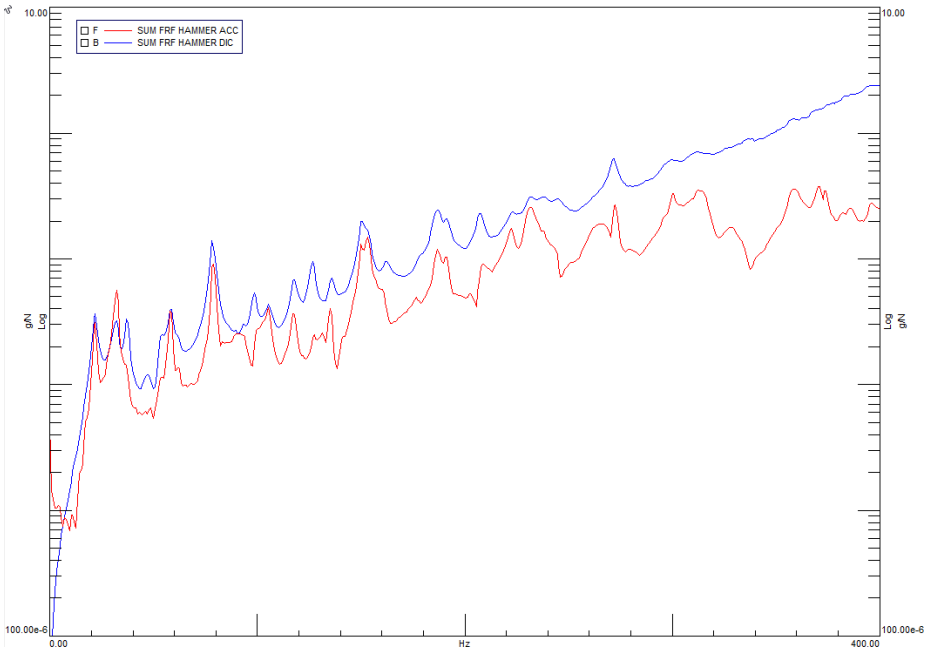

(a) Hammer test.

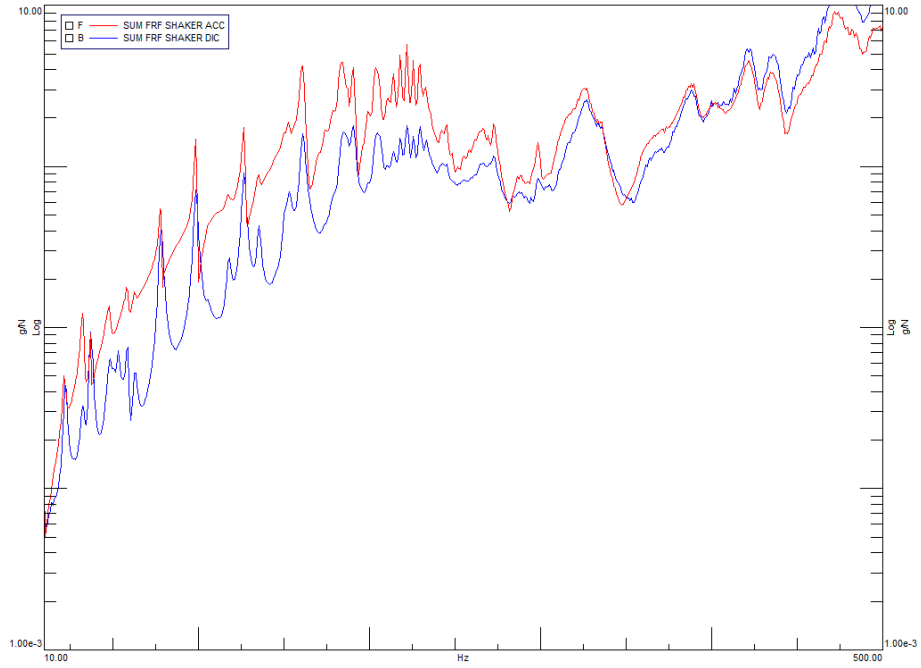

(b) Shaker test.

Figure 3.21: Comparison between the FRFs sum obtained with accelerometers and with DIC.

It is possible to notice that the two curves with the hammer test results have almost the same behaviour however, starting around 300 Hz, the DIC curve gets more flat, without any evident peak. On the shaker test result the curves are closer to each other in terms of peaks but there is a difference in the amplitude of the signal for frequencies lower than 200 Hz.

Chapter 4

Low Speed Cameras DIC on a Scaled Wind Turbine Blade

4.1 Introduction

In this chapter a scaled composite wind turbine blade, made of fiberglass and with a mass of 720 grams, is tested with two different goals. One of them is to evaluate the possibility of using low speed cameras DIC to measure the high speed behaviour of the test object and the accuracy of the results. The other is to validate the existent Finite Element Model of the scaled blade.

4.2 Finite Element Model Validation and Update

The existent model of the blade was created at Technical University of Denmark (DTU) in Simcenter 3D with a mesh of 87032 three-dimensional elements of type CHEXA(8). In order to validate it, experimental modal analysis was performed in two different boundary conditions and used to get the modal parameters of the test model. In one of the tests, with a clamped-free condition, both accelerometers and low speed cameras were used to measure the response of the system. For the other one, in a free-free condition, only the accelerometers were used. The results obtained for each situation were then correlated with the model solution in the same boundary conditions, to understand if it can be improved.

4.2.1 Boundary Condition: Clamped - Free

When the blade is assembled in the wind turbine (real condition of service) it is clamped to the rotor. To reproduce this in the test a similar situation was created with clamped-free boundary condition.

For the experimental test with this boundary conditions, the excitation was a periodic signal provided by a shaker. The system response was measured both in terms of acceleration, with accelerometers, and displacements, with DIC, using low speed cameras. Hence, the first step of the testing process was the preparation of the structure for the correlation process. The original blade, as visible in 4.1a, was completely white so, to create the required contrast to perform DIC, one of its surfaces was speckled with hand painted black dots (4.1b).

(a) Original blade.

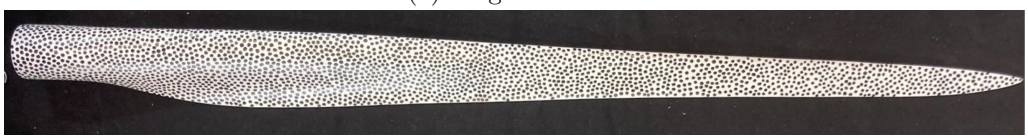

(b) Speckled blade.

Figure 4.1: Speckling process of the blade.

To measure the acceleration, 6 single axis accelerometers and 4 triaxial accelerometers were placed along the other surface, with the configuration visible in figure 4.2a. In all the points that correspond to a position of one accelerometer but on the speckled side, a sticker with a fiducial point was attached. To measure the response of the blade to the excitation provided by the shaker, a stereo DIC setup was used, with two Blackfly S BFS-U3-51S5M low speed camera whose specifications are detailed in table 4.1.

Table 4.1: Blackfly S BFS-U3-51S5M specifications.

Parameters	**Values**
Resolution	2448 x 2048 pixel
Pixel Size	3.45 μm x 3.45 μm
Maximum Frame Rate at Full Resolution	75 fps

To create the clamped-free boundary condition, the root of the blade was fixed with 6 screws to a metallic plate which was placed on a tripod, as shown in figure 4.2. The shaker was on a table and there was a load cell and an accelerometer connected to its tip and glued to the surface of the structure.

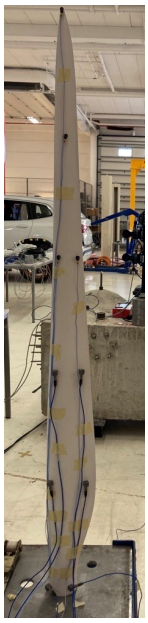

(a) Accelerometers on the blade.

(b) Experimental setup.

Figure 4.2: Experimental setup for the blade in a clamped-free condition.

The accelerometers and the force cell were connected to the acquisition system SCADAS, where their signals were recorded. The broadband signal sent to the shaker to excite the blade was also generated there. It was a periodic pseudorandom signal, with the frequency varying between 10 Hz and 400 Hz and a period of 1.28 seconds. To synchronize the cameras with the shaker, a second acquisition system, Trigger Box, interconnected with the first one was used. This is important because allows to have the input aligned with the output. To do it, a sawtooth signal, with a period of 5.12 seconds (correspondent to the 4 periods of the excitation signal that were used to average the FRFs) was generated in SCADAS and sent to the cameras through Trigger Box. The diagram in figure 4.3 summarizes this interconnection between the two acquisition systems. The information about the signal acquisition parameters is on table 4.2.

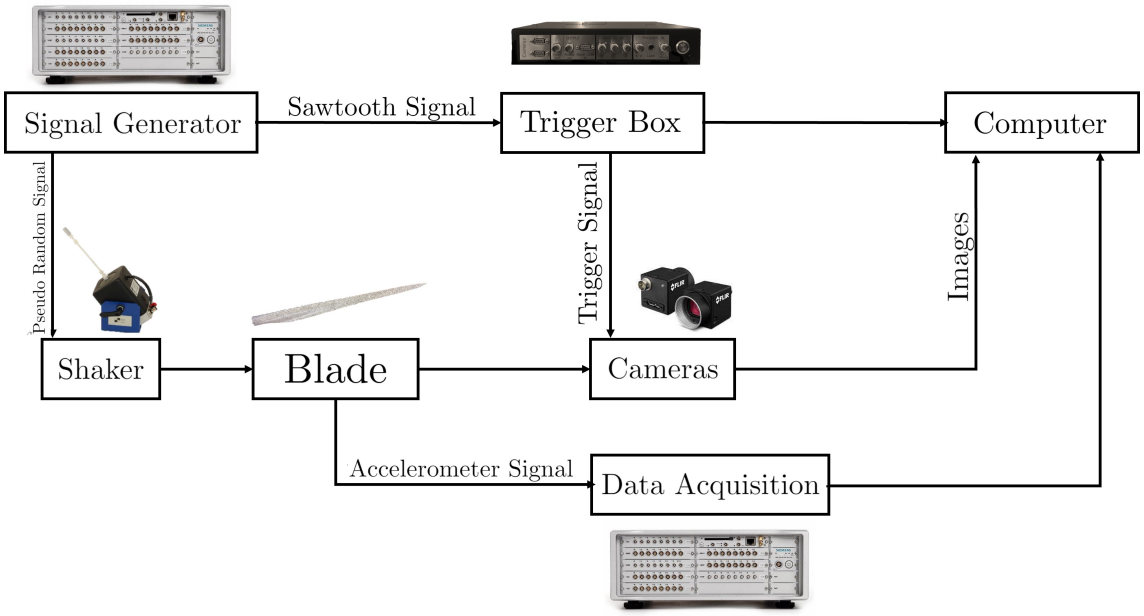

Figure 4.3: Interconnection between SCADAS and Trigger Box

Table 4.2: Acquisition parameters.

Input specification	
Parameters	*Value*
Pseudorandom Bandwidth	10-400 Hz
Pseudorandom Amplitude	0.06 V
Sawtooth Frequency	0.1953125 Hz
Sawtooth Amplitude	7.2 V
Testlab Acquisition Parameters	
Parameters	*Value*
Bandwidth	400 Hz
Sampling frequency	800 Hz
Spectral Lines	512
Acquisition Time	1.28 s
MatchID Acquisition Parameters	
Parameters	*Value*
Sampling Frequency	800 Hz
Cameras Frequency	50 Hz

It is also visible on table 4.2 that the cameras frequency is lower than the sampling frequency required to measure vibration in all the bandwidth of interest. It is supposed to reach 400 Hz which requires a sampling frequency of at least 800 Hz, according to Nyquist´s Theorem. This means that the frequencies to measure are above the Nyquist frequency of the cameras. Therefore, a reconstruction process of the signal acquired by them is needed after the test and it was done following the principle explained in section 2.3.6. The cameras take pictures with a frequency of 50 Hz which means that, in order to reach the required 800 Hz of sampling frequency, the input signal (4 pseudo random signals) has to be repeated 16 times. In each period of that signal the camera takes $5.12 \times 50 = 256$ pictures. During the complete test, 4096 pictures are acquired by each camera. After, those images are processed with Simcenter DIC software, using the correlation parameters shown in table 4.3. All the degrees of freedom were analysed and the geometry obtained directly from this process is in figure 4.4.

Table 4.3: DIC parameters.

Parameters	**Values**
Subset Size	21
Step Size	17
Interpolation Function	Bicubic Splines
Shape Function	Quadratic
Matching Criterion	ZNSSD

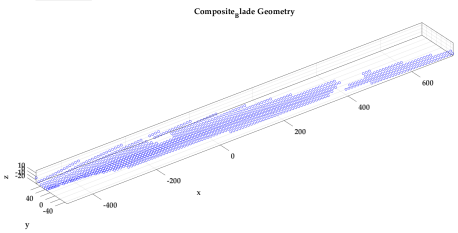

Figure 4.4: Composite blade geometry.

The displacements were extract from the Simcenter DIC software after the correlation process and imported in Matlab, where the samples were reordered to reconstruct the signal. In this way the displacement time history for each point is correct and corresponds only to one period of the sawtooth signal. The reconstructed signals are the response of each point correlated of the blade to the 4 pseudorandom signals sent to the shaker. With them, and using Matlab once again, the FRFs were calculated. For this, the signal from the load cell connected to the shaker was used as the input force. The FRFs in terms of acceleration were also calculated with the same reference in Testlab for the points with sensors, using the data acquired with SCADAS and the estimator H1.

4.2.1.1 DIC Results

The FRFs were imported in Simcenter Testlab and the stabilization diagram, that can be seen in figure 4.7, is obtained with PolyMAX Plus Tool. Using a model order of 124, 10 natural modes were found in the bandwidth of interest (10-400 Hz). The mode shapes were also calculated and the auto-MAC plotted (4.6).

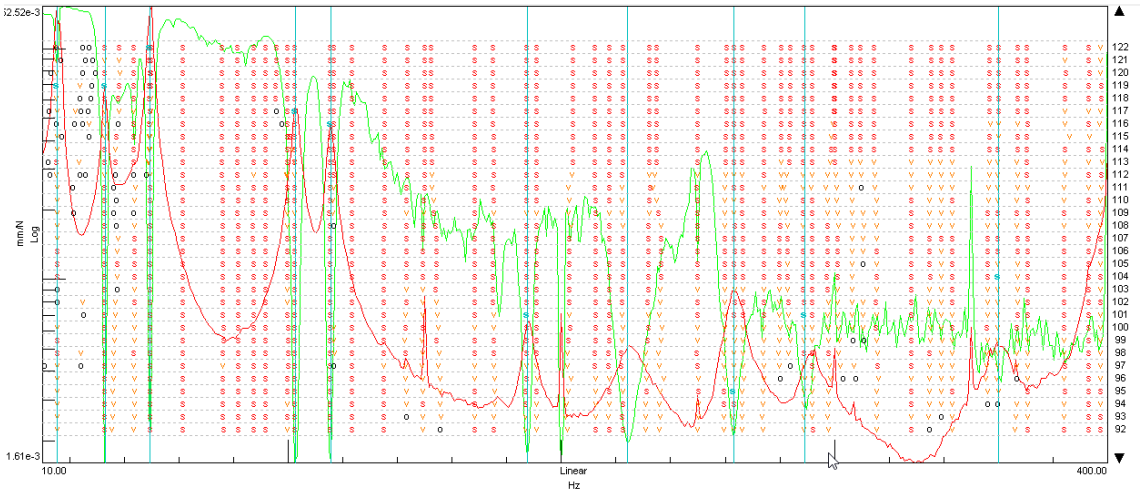

Figure 4.5: Stabilization diagram for the shaker test in clamped-free condition (DIC data).

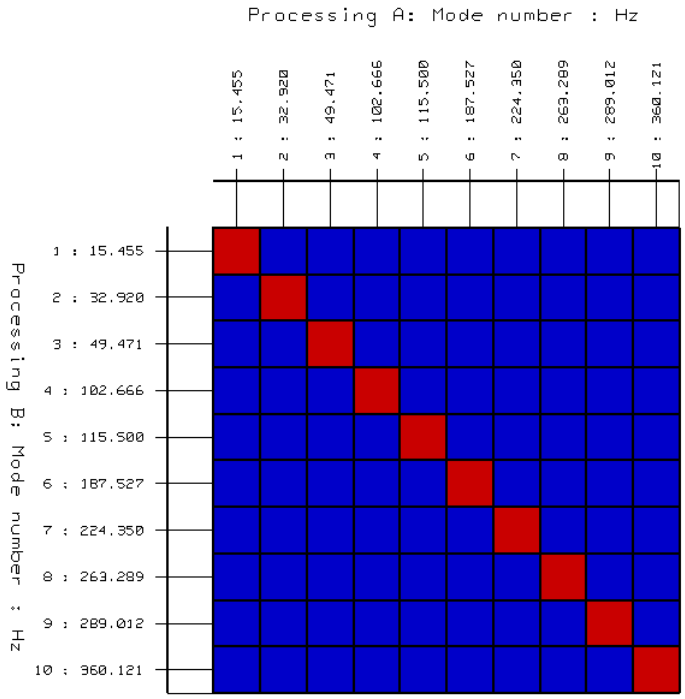

Figure 4.6: Auto-MAC for the mode set in clamped-free condition (DIC data).

4.2.1.2 Accelerometers Results

The geometry of the blade in Simcenter Testlab was created based on the real positioning of the accelerometers along the surface. Comparing one picture acquired in a static condition with the geometry extracted directly from the Simcenter DIC software it is possible to locate the points with the fiducial points. Then they are picked and their coordinates used to select the correspondent ones on the FE model. The points in the model that are in the same position but in the opposite surface are chosen as the points where the accelerometers are. The coordinates of each point are imported in Testlab and used as nodes for the geometry. This allows to have an accurate position of each point where the FRFs are calculated, leading to accurately determined mode shapes.

Using PolyMAX Tool on Simcenter Testlab, the stabilization diagram was obtained and can be seen in figure 4.7 together with the selected natural modes for the blade in clamped-free condition. Between 10 Hz and 400 Hz, with a model order of 32, 10 natural modes were found and the respective mode shapes calculated. The auto-MAC for this mode set is in figure 4.8.

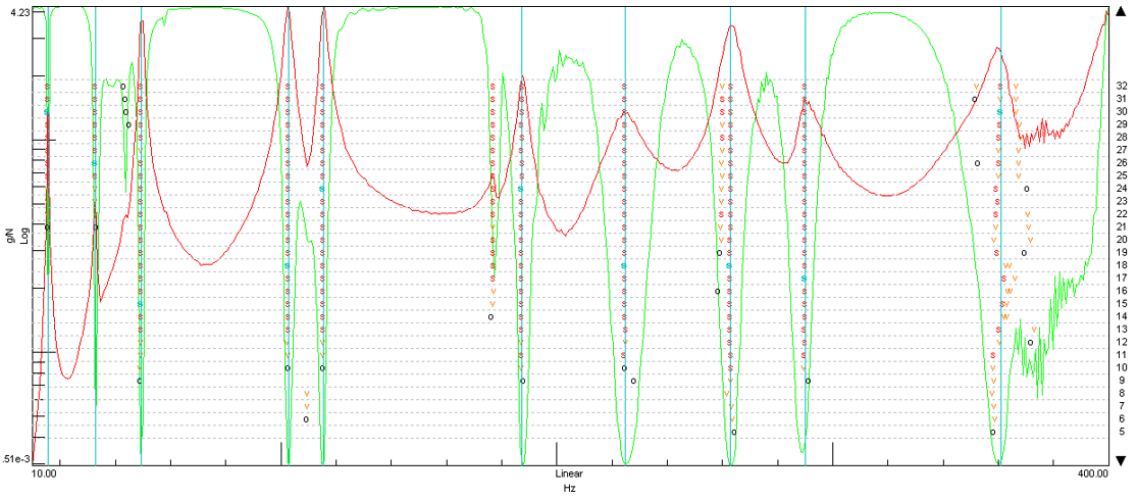

Figure 4.7: Stabilization diagram for the shaker test in clamped-free condition (accelerometers data).

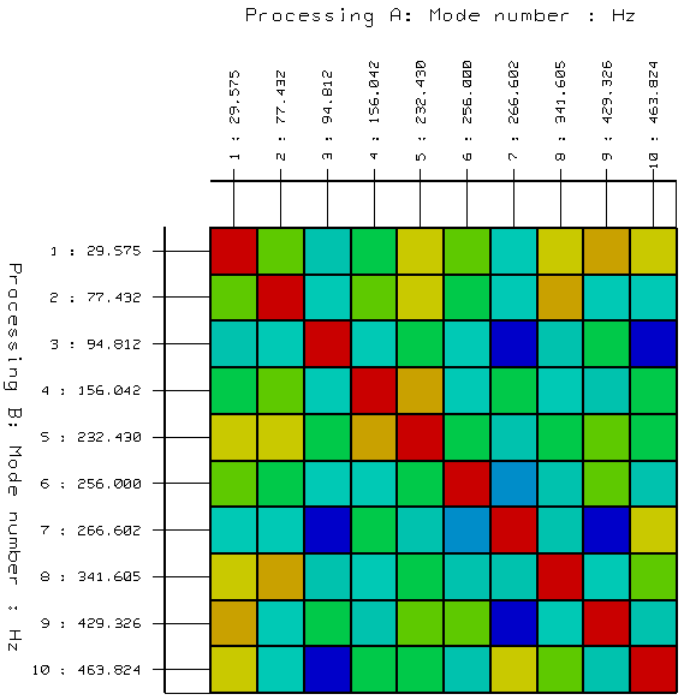

Figure 4.8: Auto-MAC for the mode set in clamped-free condition (accelerometers data).

4.2.1.3 Comparison Between Accelerometers and DIC Results

From the FRFs point of view, and when comparing the sum of the FRFs obtained with the accelerometers data and the sum of the ones obtained using DIC (both plotted in figure 4.9) it is possible to see that DIC data is noisier, specially close the harmonic frequencies of the cameras. To have the two curves on the same plot and with the same units the FRF sum obtained with DIC, in mm/N, was double differentiated.

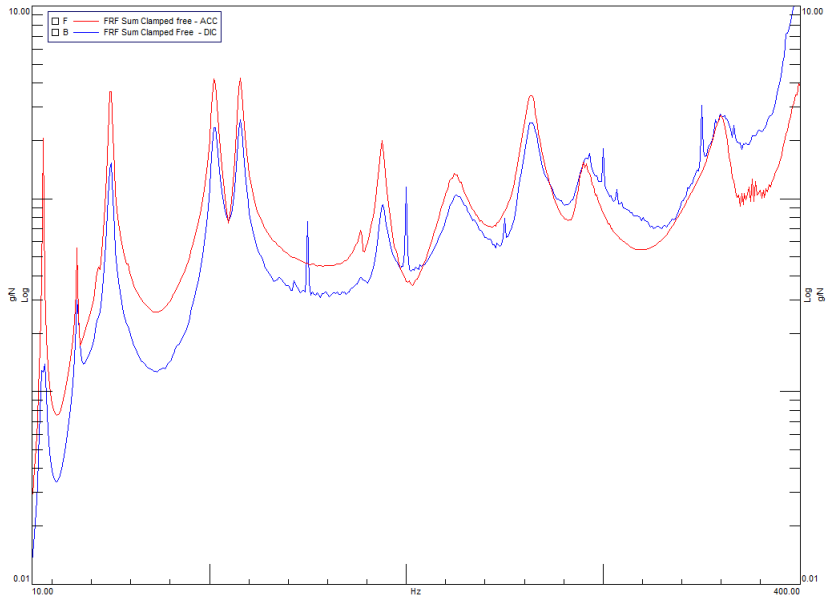

Figure 4.9: FRF sums obtained with accelerometers data and with DIC.

The cameras speed was 50 frames per second during the test and the peaks at frequencies that are multiples of 50 do not represent real natural modes of the structure. The noise is also evident at the higher frequencies, as expected from the state of the art. Nevertheless, it can be noticed that the peaks are all at the same frequencies. This is also demonstrated by the very small error between the natural frequencies obtained with the accelerometers and with DIC, presented for each mode in table 4.4. The table shows also the error between the damping ratio for each mode in the two different mode sets.

Table 4.4: Comparison between natural frequencies and damping ratios.

Mode	**Natural frequencies**			**Damping ratios**		
	Acc [Hz]	*DIC [Hz]*	*Error [%]*	*Acc [%]*	*DIC [%]*	*Error [%]*
1	15.54	15.46	0.51	0.59	3.21	444.07
2	32.89	32.93	0.12	1.82	2.20	20.88
3	49.56	49.48	0.16	1.45	2.05	41.38
4	102.64	102.67	0.03	1.37	1.37	0.00
5	115.38	115.50	0.10	1.14	1.17	2.63
6	187.46	187.53	0.04	1.11	1.01	9.01
7	224.75	224.35	0.18	2.53	0.23	90.91
8	262.95	263.29	0.13	1.13	0.20	82.30
9	290.00	289.01	0.34	1.39	0.46	66.91
10	360.82	360.12	0.19	2.50	0.18	92.80

The results obtained for the modal analysis of the composite blade using DIC with low speed cameras are very accurate in terms of natural frequencies. The error, calculated using the values obtained with the accelerometers as reference, is always lower than 1%. The error for the damping ratios calculated with DIC, using the ones calculated with the accelerometers results as reference varies a lot along the mode set, being a bit unpredictable, but is very high for some modes. The reason of this is probably the same that was mentioned for the tests with high speed cameras.

From the auto-MAC point of view it is possible to conclude that the level of correlation between modes out of the diagonal in the mode set obtained with the accelerometers is higher than the same value for the mode set calculated with DIC. These data resulted from the same test so this is mainly due to the fact that in the accelerometers data set there are few points to compare between modes.

4.2.1.4 FEA Results

The mass of the accelerometers used during the test has to be contemplated in the finite element model because of its influence on the modal parameters that are supposed to be compared, special because the composite blade is a very light structure. The mass of the model is 695.2 grams. This was done adding 10 Concentrated Mass Elements (zero dimensions elements) in the points where they were placed in the test model, with the mass of the correspondent sensor. The mass of each one of the 4 triaxial accelerometers used is 1.5 grams, the mass of 2 of the 6 single axis is 4.5 grams and for the other 4 it is 1 gram per each. The total mass added to the model for the sensors was 19 grams.

To create the clamped-free condition of the blade in the finite element model, the root was fixed by six CBUSH elements to simulate the six screws used during the test. This is visible in figure 4.10a. 6 nodes were added to the mesh in the points where the center of the holes are in the real blade. One of the ends of each CBUSH element was connected to one of this nodes. Other 6 nodes were created away from the bottom surface to connect the second end of the CBUSH and it was used a constrain for the 3 translation DOF on these nodes. The nodes on the surface were also linked to the bottom edges through RBE2 elements, as shown in figure 4.10b.

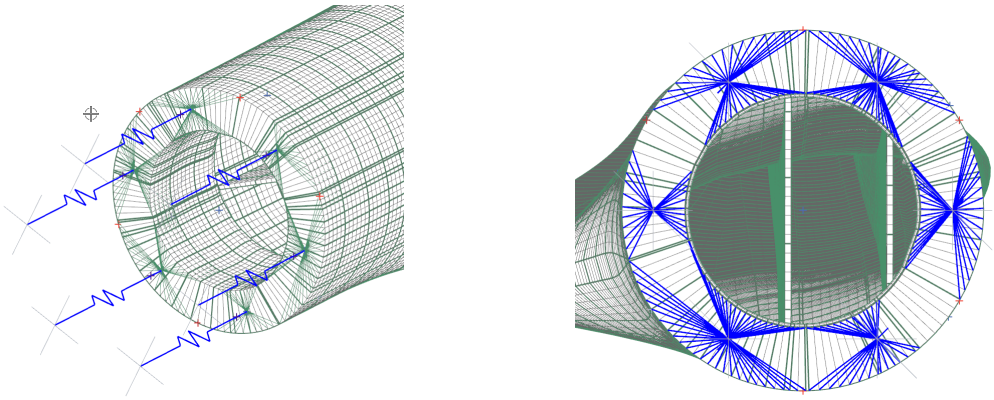

(a) CBUSH elements. (b) RBE2 elements.

Figure 4.10: Clamping solution on the blade model.

Adjusting the stiffness of the CBUSH elements is a way of reproduce the strength applied in the bolt connection of the testing model. The best value is the one that returns the natural frequencies closer to the ones found with the experimental test and does not reduce the MAC values too much, so the correlation of the mode shapes is still good. That value was defined on a trial and error base and the option was 14000 N/mm for the 3 translation degrees of freedom. Other option to do this could be using a different software to perform an optimization algorithm for the laminate composite models in order to match the natural frequencies obtained in the simulation with the ones from the experimental

model. However, due to the lack of time, and the computational effort of processing the model of the blade, the optimization process was done manually.

The solver SOL 103 Real Eigenvalues of Simcenter 3D was used to calculate the first 10 natural frequencies of the blade with the clamped-free boundary condition and the respective mode shapes. These modes were correlated with the ones previously calculated in Testlab, with the result from the experimental modal analysis, with DIC and with accelerometers. It is important to note that to perform this correlation, the test mode set has to be calculated in the real format and then the geometry is exported in a different file of the one with the natural frequencies and the mode shapes. After importing these files in Simcenter 3D, the two models (the experimental and the numerical) have to be aligned because normally they are not in the same referential.

4.2.1.5 Correlation with Accelerometers Mode Set

The results of the correlation between the numerical solution and the experimental test with the accelerometers data both in terms of MAC matrix and natural frequencies comparison are shown in figure 4.11 and table 4.5.

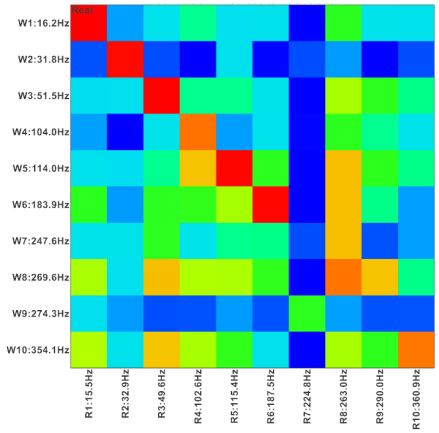

Figure 4.11: MAC matrix for clamped-free condition - accelerometers data.

Table 4.5: Comparison between test and simulation - accelerometers data.

Mode	**Natural Frequency**			**MAC**
	Test [Hz]	*Model* [Hz]	*Error* [%]	
1	15.54	16.19	4.18	0.99
2	32.89	31.78	3.38	0.91
3	49.56	51.52	3.96	0.98
4	102.64	104.02	1.34	0.89
5	115.38	114.03	1.17	0.95
6	187.46	183.89	1.90	0.93
7	224.75	247.64	10.19	0.12
8	262.95	269.61	2.53	0.84
9	290	274.26	5.43	0.19
10	360.82	354.06	1.87	0.81

Looking to the comparison between the natural frequencies obtained with the two methods it is possible to say that there is a good correspondence for this parameter except for the modes number 7 and number 9, where the error is higher than 5%. Also from the MAC point of view the same conclusion is drawn. The MAC values are almost all above 0.8, indicating good correlation between the mode shapes but for the modes number 7 and 9 this value is close to zero, meaning that the modes are not well correlated. When analysing these two modes shapes from the numerical point of view and comparing with the ones obtained with the accelerometers one can understand that they are both torsional

modes. This problem will be detailed on the next paragraph because it is more evident when comparing the numerical mode shapes with the ones calculated with DIC. The MAC values out of the diagonal are acceptable except in very specific combinations, most of them including the mode number 8. However, when the goal is to validate a model uses to be enough to correlate the modes up to the first torsional one which is,in this case, the mode number 7. If only that part of the MAC matrix is analysed then is visible to conclude that the values are good so the model does not need to be updated.

4.2.1.6 Correlation with DIC Mode Set

The numerical solution for the clamped-free condition was also correlated with the modes obtained with DIC data during the experimental test. The results of this process, in terms of MAC, error between the natural frequencies and comparison between mode shapes can be seen in figure 4.12, table 4.6 and figure 4.13 respectively.

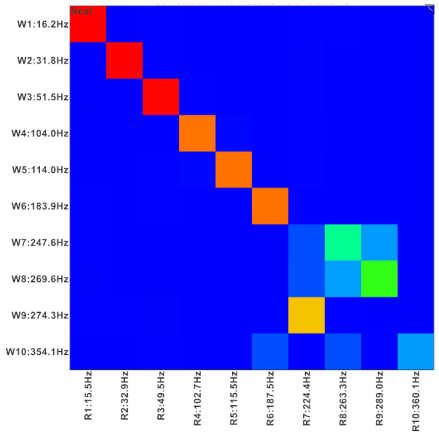

Figure 4.12: MAC matrix for clamped-free condition - DIC data.

Table 4.6: Comparison between test and simulation - DIC data.

Mode	**Natural Frequency**			**MAC**
	Test [Hz]	*Model* [Hz]	*Error* [%]	
1	15.46	16.19	4.72	0.99
2	32.93	31.78	3.49	0.99
3	49.48	51.52	4.12	0.95
4	102.67	104.02	1.31	0.86
5	115.5	114.03	1.27	0.90
6	187.53	183.89	1.94	0.89
7	224.35	247.64	10.38	0.11
8	263.29	269.61	2.405	0.28
9	289.01	274.26	5.10	0.00
10	360.12	354.06	1.68	0.26

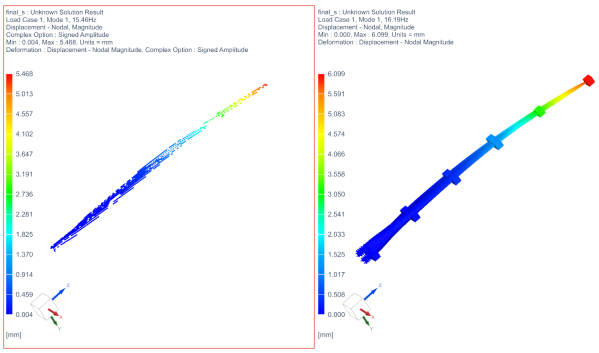

(a) 1^{st} experimental mode - 1^{st} numerical mode

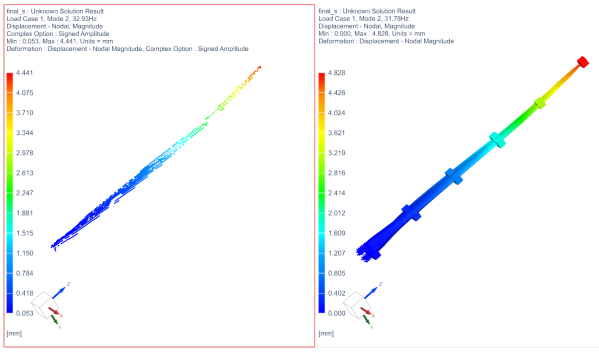

(b) 2^{nd} experimental mode - 2^{nd} numerical mode

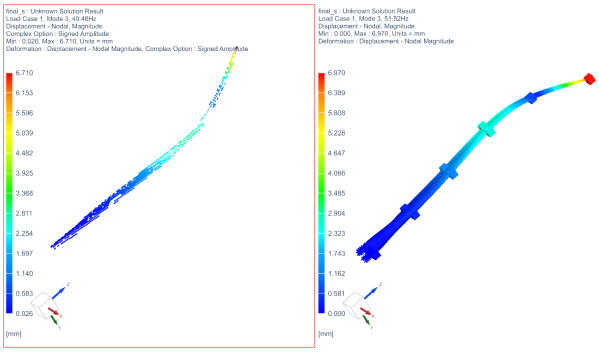

(c) 3^{rd} experimental mode - 3^{rd} numerical mode

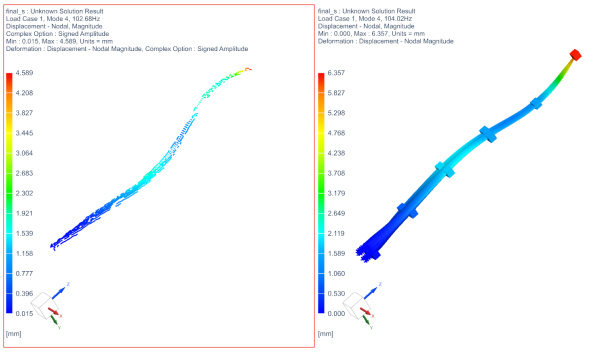

(d) 4^{th} experimental mode - 4^{th} numerical mode

Figure 4.13: Comparison between experimental and numerical natural modes.

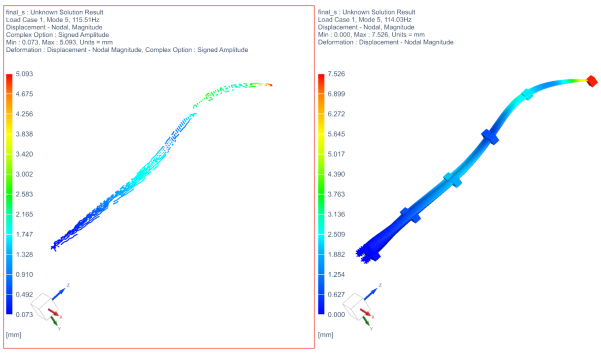

(e) 5^{th} experimental mode - 5^{th} numerical mode

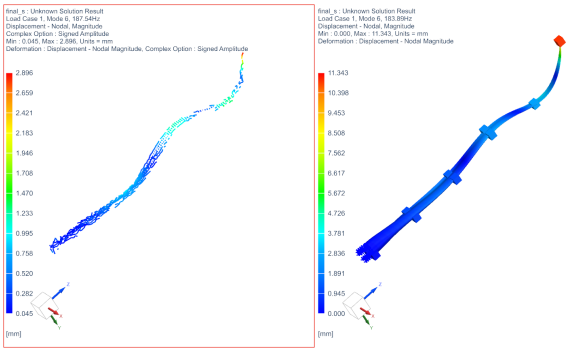

(f) 6^{th} experimental mode - 6^{th} numerical mode

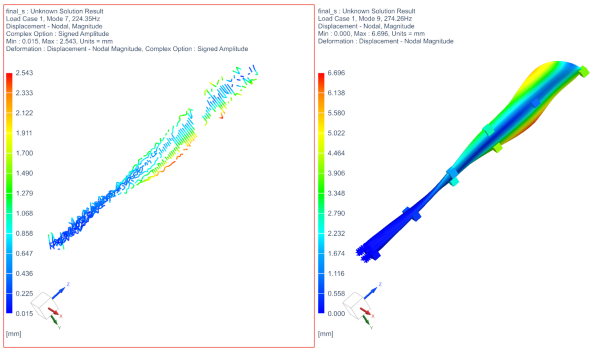

(g) 7^{th} experimental mode - 9^{th} numerical mode

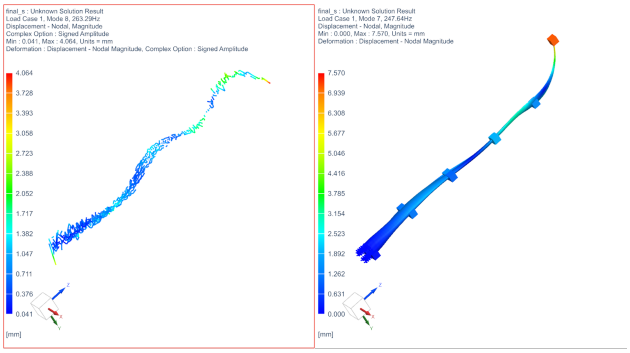

(h) 8^{th} experimental mode - 7^{th} numerical mode

Figure 4.13: Comparison between experimental and numerical natural modes.

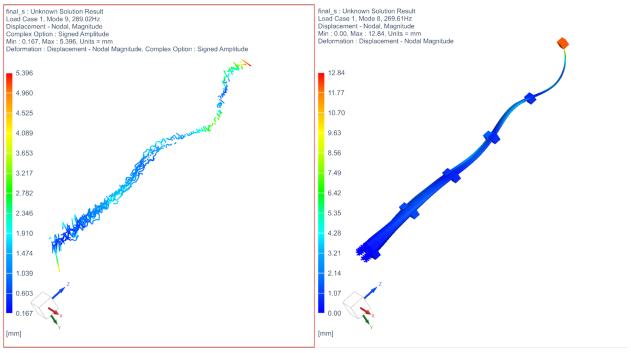

(i) 9^{th} experimental mode - 8^{th} numerical mode

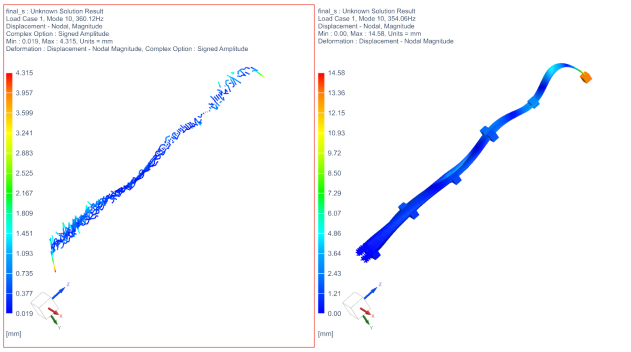

(j) 10^{th} experimental mode - 10^{th} numerical mode

Figure 4.13: Comparison between experimental and numerical natural modes.

From the natural frequencies point of view, the results of the model correlation with the accelerometers data set or with the DIC data set are almost the same, with the errors being very similar. When observing the MAC plotted, and comparing it to the one obtained for the correlation with the accelerometers data set (figure 4.11), it is possible to see that it improved. The values out of the diagonal are almost all close to zero, what does not happen in the other situation. However, it is visible a decrease of the MAC value on the diagonal, more evident at high frequencies. With this data set, the last 4 natural modes do not correlate with the ones in the finite element model, with MAC values close to zero. One aspect to highlight is that, according to the MAC matrix, these last modes are not correlated by the natural frequency order. The mode number 7 on the experimental data set (the first torsional mode) is correlated with the mode number 9 on the numerical model, the mode number 8 on the test is correlated with the mode number 7 of the model and the mode number 9 of the test is correlated with the mode number 8 on the model. The mode number 10 on the experimental data set is correlated with the number 10 in the model but with a low MAC value (0.26).

In order to try to understand the points where the correlation is poorer and that were impacting the results, making the MAC values very low at high frequencies, the CoMAC was calculated for the last 4 modes for each degree of freedom. The resultant plot is in figure 4.14.

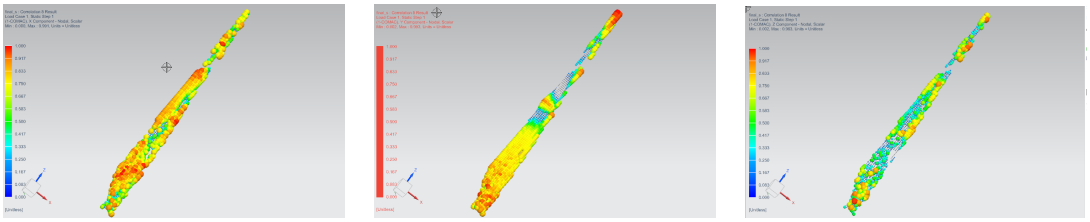

(a) CoMAC - X direction. (b) CoMAC - Y direction. (c) CoMAC - Z direction.

Figure 4.14: CoMAC for the last 4 modes.

Here, as well as in the MAC, red stands for a value of 1 while dark blue stands for 0. In other words, the red (and bigger) dots are in the points where the correlation is better. Analysing these results one can conclude that the directions X and Y have the best correlation values for the high frequency modes and that the worst degree of freedom is the Z direction, where the correlation values are lower (mostly populated with blue and small dots). Also, the critical section is the middle one.

From the mode shapes it is visible that the last for modes are almost in the out of plane direction (Y in the model) so the correlation process was done again considering only this degree of freedom, to understand if it can improve the correlation values for these modes. The resultant MAC is plotted in figure 4.15 and the values along the diagonal can be seen in table 4.7.

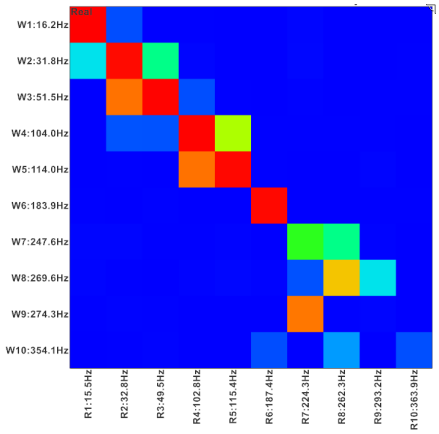

Figure 4.15: MAC matrix for clamped-free condition considering only the out of plane direction.

Table 4.7: MAC values on the diagonal.

Mode	MAC Value
1	1
2	0.901
3	0.972
4	0.977
5	0.934
6	0.918
7	0.533
8	0.703
9	0.082
10	0.141

The MAC values on the diagonal when the correlation is performed considering just the out of plane degree of freedom are better than when considering them all. The biggest difference is on the 7^{th} and 8^{th} modes where the MAC value increased from 0.11 to 0.53 and from 0.28 to 0.70, respectively. This can mean that the boundary condition on the in plane directions is not fully representative of the reality.

4.2.2 Boundary Condition: Free - Free

To simulate the free free condition in the test environment, the blade was suspended by soft bungees on a metallic frame. To excite the structure, an ICP impact hammer model 086C03 from PCB was used. The accelerometers used to measured the response were the same ones and were placed in the same positions as in the shaker test for the clamped-free condition. The impact hammer and the sensors were connected to the acquisition system SCADAS, where their signals were recorded. The setup for the hammer test can be seen in figure 4.16.

Figure 4.16: Experimental setup for the hammer test.

The tip chosen for the impact hammer allowed to excite the structure up to a frequency close to 512 Hz so this was the bandwidth used for the test. The sample frequency was 1024 Hz and the resolution was 0.5 Hz. Hence, the acquisition time was 2 seconds.

The geometry of the blade was created in Testlab based on the position of the accelerometers, and it was the same as in the shaker test for the clamped-free condition. With the acceleration data for the 10 points with sensors as the output and the force measured by the hammer as the input, the FRFs were calculated. This was done with Simcenter Testlab and using the estimator H1.

4.2.2.1 Accelerometers Results

The stabilization diagram obtained with PolyMAX tool using a model order of 40 is shown in figure 4.17 where it is also possible to see the natural modes selected. In the bandwidth of interest 10 natural modes of vibration were found and the respective mode shapes were calculated.

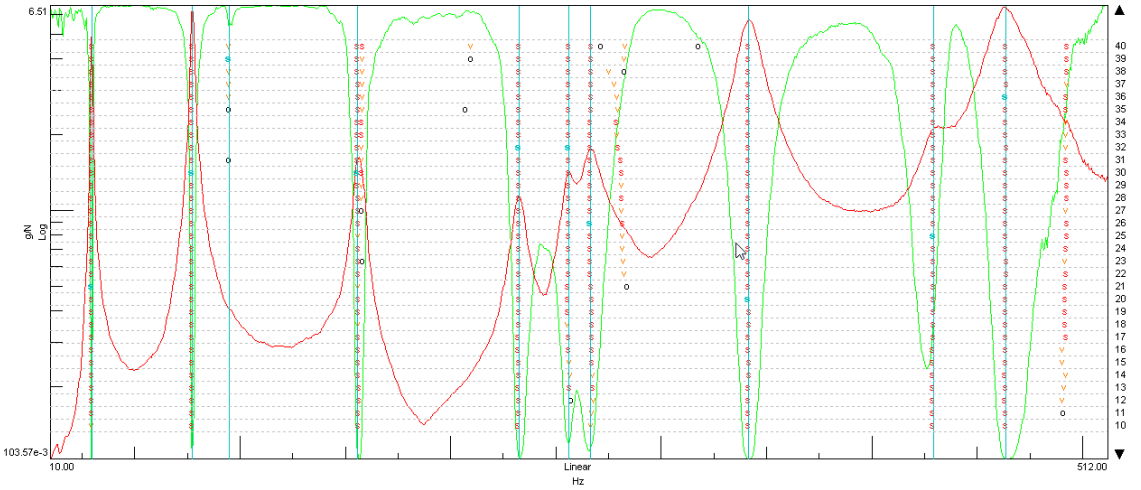

Figure 4.17: Stabilization diagram for the hammer test in free-free condition.

Because of the non periodic behavior of the impact hammer excitation, it is not possible to use DIC with low speed cameras to measure vibration at high frequencies since that it requires a reconstruction process of the signals based on the repeatably of the test, as already explained.

4.2.2.2 Correlation with Accelerometers Mode Set

Using the SOL 103 Real Eigenvalues in Simcenter 3D the natural frequencies and the mode shapes for the blade in free-free condition (without any constraint and without the CBUSH and RBE2 elements) were calculated. Up to 500 Hz the model has 11 natural modes that were correlated with the ones found with the experimental test. These modes were also compared from the natural frequency point of view, and the error. The resultant MAC is in figure 4.18. The comparison between the natural modes obtained for the finite element model and the ones obtained for the experimental model in terms of natural frequencies in table 4.8 and in terms of mode shapes in figure 4.19.

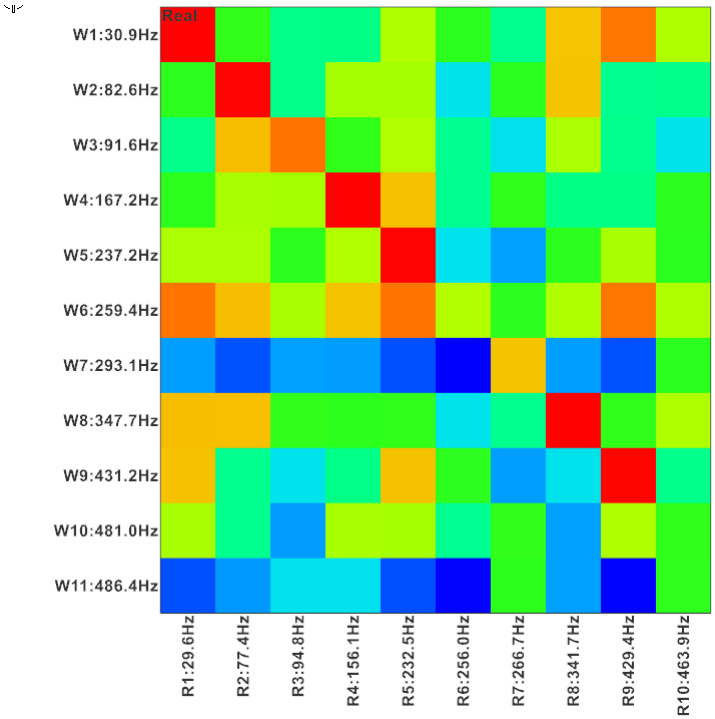

Figure 4.18: MAC matrix for free-free condition.

Table 4.8: Comparison between test and simulation - accelerometers data.

Mode	**Natural Frequency**			**MAC**
	Test [Hz]	*Model* [Hz]	*Error* [%]	
1	29.6	30.9	4.3	0.99
2	77.4	82.6	6.7	0.97
3	94.8	91.6	3.4	0.87
4	156.1	167.2	7.1	0.99
5	232.5	237.2	2.0	0.96
6	256.0	259.4	1.3	0,69
7	266.7	293.1	9.9	0.71
8	341.7	347.7	1.8	0.98
9	429.4	431.2	0.4	0.95
10	463.9	481.0	3.7	0.58

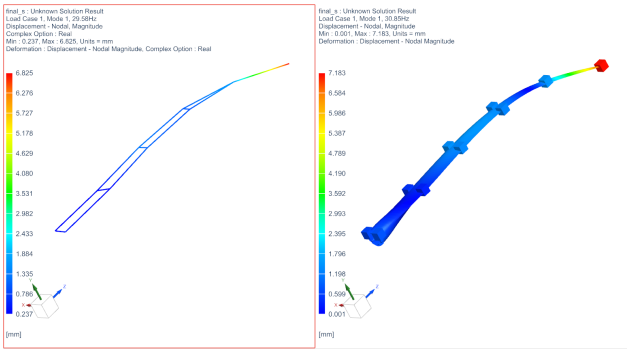

(a) 1^{st} experimental mode - 1^{st} numerical mode

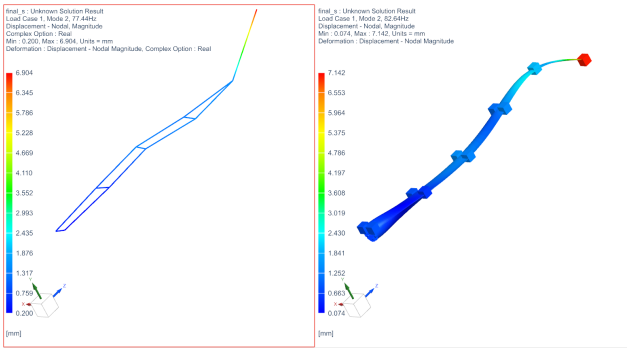

(b) 2^{nd} experimental mode - 2^{nd} numerical mode

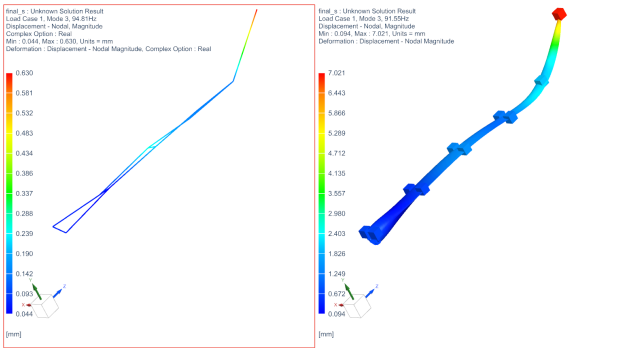

(c) 3^{rd} experimental mode - 3^{rd} numerical mode

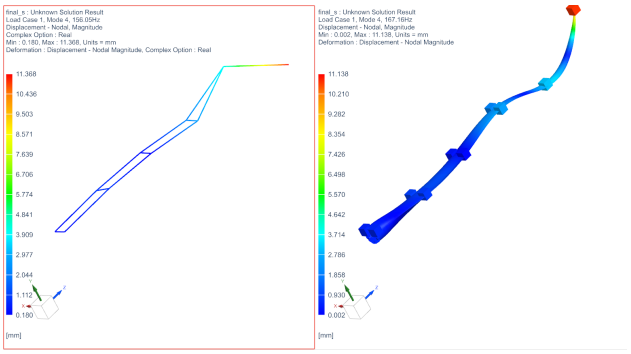

(d) 4^{th} experimental mode - 4^{th} numerical mode

Figure 4.19: Comparison between experimental and numerical natural modes.

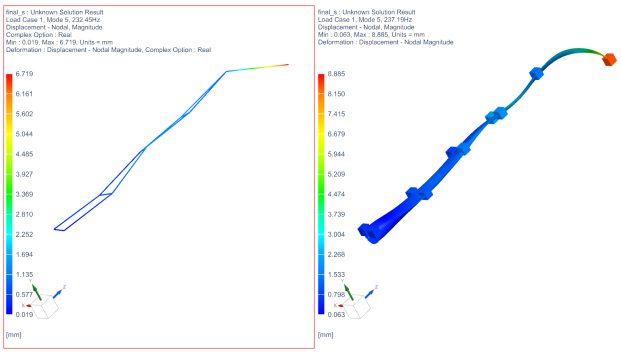

(e) 5^{th} experimental mode - 5^{th} numerical mode

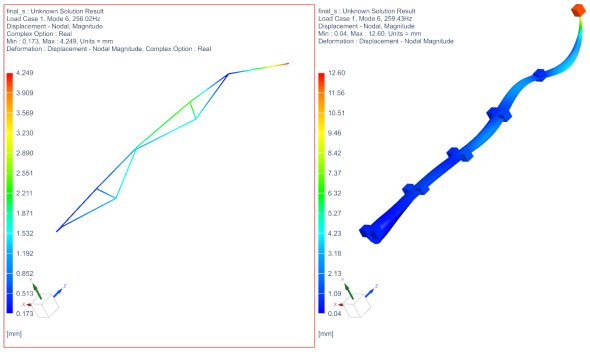

(f) 6^{th} experimental mode - 6^{th} numerical mode

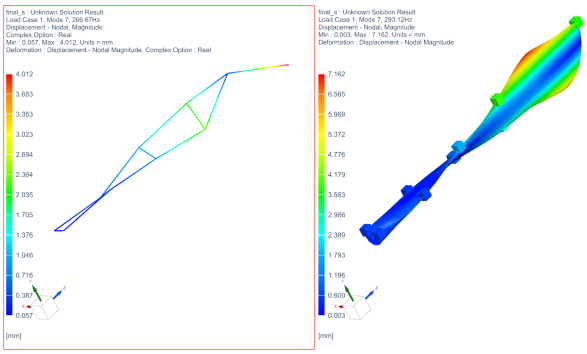

(g) 7^{th} experimental mode - 7^{th} numerical mode

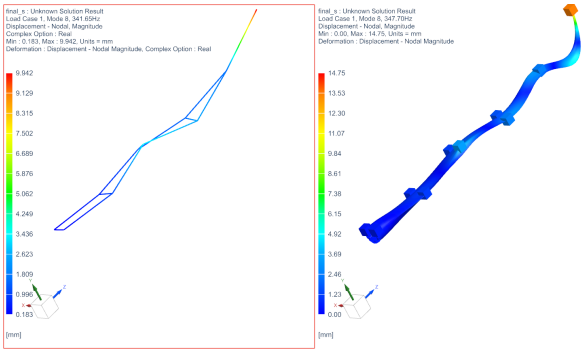

(h) 8^{th} experimental mode - 8^{th} numerical mode

Figure 4.19: Comparison between experimental and numerical natural modes.

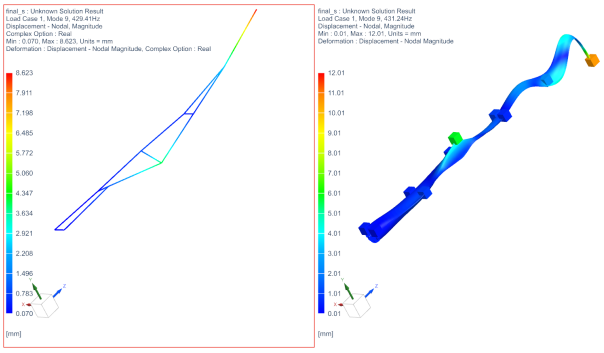

(i) 9^{th} experimental mode - 9^{th} numerical mode

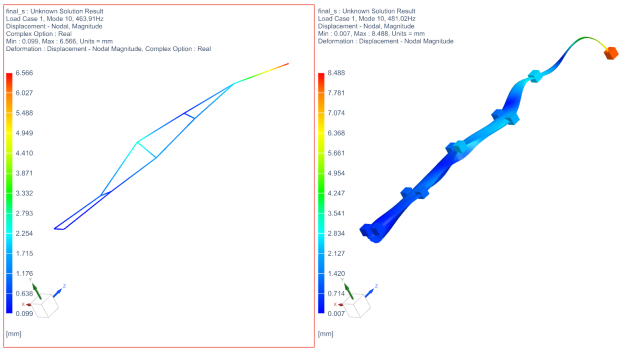

(j) 10^{th} experimental mode - 10^{th} numerical mode

Figure 4.19: Comparison between experimental and numerical natural modes.

It is visible that there is a good correlation when comparing the numerical mode shapes and the experimental ones for the 9 first modes, with the MAC values always above 0.69 and very close to 1 for the most of them. The error between the natural frequencies obtained from the finite element model and the ones that were found with the experimental test is a bit higher than expected for some modes. This is probably due to the difference between the mass of the model and the mass of the manufactured blade that was used to perform the test. Can be also an effect of the boundary conditions because the blade is very light and even using very soft bungees it´s not possible to say that it is completely free.

Chapter 5

Conclusion

5.1 Conclusions

After all the work and research developed throughout this thesis, several conclusions were formed.

With the tests performed on the dryer machine it was possible to verify that digital image correlation with high speed cameras is a good alternative to the traditional point-wise sensors to retrieve the natural frequencies and mode shapes of a structure. The errors between the natural frequencies obtained with this method and the ones obtained using accelerometers to measure the response of the structure are always very low. The same does not happen for the damping ratios, where the error can assume either very low or very high values. At high frequencies, DIC is not so reliable because the measurements start getting very noisy.

When testing the wind turbine blade to validate its finite element model, it was concluded that using low speed cameras to acquire the pictures is also an option since the results, in terms of natural frequencies and modes shapes, are very close to the ones obtained with accelerometers used as reference. However, this method requires one more step in the post processing phase, regarding the signal reconstruction. The scaled model of the blade use for testing was a very light structure and that highlighted the influence of the mass of the sensors in the modal parameters found.

DIC is a powerful tool to validate finite element models due to its accuracy and full field measuring capability. After the correlation process it was possible to say that the model was good, with acceptable MAC values for the two different boundary conditions studied. The differences noticed between the natural frequencies were due to the differences in the mass of the finite element model and the experimental model.

5.2 Future Work

Considering the work done in this thesis and the results obtained, some developments can be made to improve them. Also, more tests can be performed to investigate the potential of DIC in different conditions. Some of those suggestions, as future steps remarks, are the following:

- Use a FEM optimization software to update the wind turbine blade model and get a better match between its natural frequencies and mode shapes and the ones obtained experimentally;
- Perform sensitivity analysis on the setup parameters such as the cameras settings and relative angles to reduce the noise floor and increase the reachable bandwidth
- Implement data reduction techniques to reduce the computational effort of the correlation process and the time associated to it;
- Test the blade on the rotating wind turbine to investigate the accuracy of DIC for modal analysis on rotating structures.

References

[1] D. J. Ewins, *Modal Testing: Theory, Practice and Application*. John Wiley Sons, 2nd ed., 2009.

[2] J. Baqersad, P. Poozesh, C. Niezrecki, and P. Avitabile, "Photogrammetry and optical methods in structural dynamics – A review," *Mechanical Systems and Signal Processing*, vol. 86, pp. 17–34, 2017.

[3] A. Zanarini, "Full field optical measurements in experimental modal analysis and model updating," *Journal of Sound and Vibration*, vol. 442, pp. 817–842, 2019.

[4] D. Francis, R. P. Tatam, and R. M. Groves, "Shearography technology and applications: A review," *Measurement Science and Technology*, vol. 21, no. 10, 2010.

[5] O. J. Løkberg, "ESPI—The ultimate holographic tool for vibration analysis?," *Journal of the Acoustical Society of America*, vol. 75, no. 6, pp. 1783–1791, 1984.

[6] J. Monteiro, J. Chouzal, M. Vaz, and R. dos Bragas, "Vibration analysis by laser interferometry techniques," in *Congress on Aeronautical Technologies, Covilhã*, 1997.

[7] P. L. Reu, D. P. Rohe, and L. D. Jacobs, "Comparison of DIC and LDV for practical vibration and modal measurements," *Mechanical Systems and Signal Processing*, vol. 86, pp. 2–16, 2017.

[8] B. L. Witt and D. P. Rohe, "Digital Image Correlation as an Experimental Modal Analysis Capability," *Experimental Techniques*, vol. 45, no. 3, pp. 273–286, 2021.

[9] J. Winstroth, L. Schoen, B. Ernst, and J. R. Seume, "Wind turbine rotor blade monitoring using digital image correlation: A comparison to aeroelastic simulations of a multi-megawatt wind turbine," *Journal of Physics: Conference Series*, vol. 524, no. 1, 2014.

[10] P. Poozesh, A. Sabato, A. Sarrafi, C. Niezrecki, and P. Avitabile, "A Multiple Stereo-Vision Approach Using Three-Dimensional Digital Image Correlation for Utility-Scale Wind Turbine Blades," no. March, pp. 8–11, 2018.

[11] P. Sousa, P. Barros, F. Tavares, and P. Moreira, "Displacement measurement and shape acquisition of an RC helicopter blade using Digital Image Correlation,"

[12] S. Galeazzi, P. Chiariotti, M. Martarelli, and E. P. Tomasini, "3D Digital Image Correlation for vibration measurement on rolling tire: Procedure development and comparison with Laser Doppler Vibrometer," *Journal of Physics: Conference Series*, vol. 1149, no. 1, 2018.

[13] A. Yashar, N. Ferguson, and M. G. Tehrani, "Measurement of rotating beam vibration using optical (DIC) techniques," *Procedia Engineering*, vol. 199, pp. 477–482, 2017.

[14] T. E. Schmidt, J. Tyson, K. Galanulis, D. M. Revilock, and M. E. Melis, "Full-field dynamic deformation and strain measurements using high-speed digital cameras," *26th International Congress on High-Speed Photography and Photonics*, vol. 5580, p. 174, 2005.

[15] J. Javh, M. Brumat, J. Slavič, and M. Boltežar, "A high-speed camera measurement set-up for deflection shape analysis," *Proceedings of ISMA 2016 - International Conference on Noise and Vibration Engineering and USD2016 - International Conference on Uncertainty in Structural Dynamics*, no. March 2017, pp. 1043–1050, 2016.

[16] J. Javh, J. Slavič, and M. Boltežar, "Full-field modal analysis using a DSLR camera," *Conference Proceedings of the Society for Experimental Mechanics Series*, vol. 6, pp. 27–30, 2019.

[17] D. Mastrodicasa, E. Di Lorenzo, B. Peeters, and P. Guillaume, "A demo airplane full field modal validation using digital image correlation," *Proceedings of ISMA 2020 - International Conference on Noise and Vibration Engineering and USD 2020 - International Conference on Uncertainty in Structural Dynamics*, 2020.

[18] D. Mastrodicasa, E. D. Lorenzo, S. Manzato, B. Peeters, and P. Guillaume, "Combining pointwise sensors and DIC for modal analysis Low speed camera for high frequency behaviour characterization,"

[19] J. Javh, J. Slavič, and M. Boltežar, "High frequency modal identification on noisy high-speed camera data," *Mechanical Systems and Signal Processing*, vol. 98, pp. 344–351, 2018.

[20] B. LeBlanc, C. Niezrecki, P. Avitabile, J. Chen, and J. Sherwood, "Damage detection and full surface characterization of a wind turbine blade using three-dimensional digital image correlation," *Structural Health Monitoring*, vol. 12, no. 5-6, pp. 430–439, 2013.

[21] S. Catt, B. Fick, M. Hoskins, J. Praski, and J. Baqersad, "Development of a semi-autonomous drone for structural health monitoring of structures using digital image correlation (DIC)," *Conference Proceedings of the Society for Experimental Mechanics Series*, vol. 6, no. Dic, pp. 49–57, 2019.

[22] T. J. Beberniss and D. A. Ehrhardt, "High-speed 3D digital image correlation vibration measurement: Recent advancements and noted limitations," *Mechanical Systems and Signal Processing*, vol. 86, pp. 35–48, 2017.

[23] D. Lecompte, A. Smits, S. Bossuyt, H. Sol, J. Vantomme, D. Van Hemelrijck, and A. M. Habraken, "Quality assessment of speckle patterns for digital image correlation," *Optics and Lasers in Engineering*, vol. 44, no. 11, pp. 1132–1145, 2006.

[24] D. Lecompte, H. Sol, J. Vantomme, and A. Habraken, "Analysis of speckle patterns for deformation measurements by digital image correlation," *Speckle06: Speckles, From Grains to Flowers*, vol. 6341, p. 63410E, 2006.

[25] W. Heylen, S. Lammens, and P. Sas, *Modal Analysis Theory and Testing*. Leuven: Katholieke Universiteit Leuven, Faculty of Engineering, Department of Mechanical Engineering, Division of Production Engineering, Machine Design and Automation, 1998.

[26] D. Rodrigues, *Apontamentos de Vibrações de Sistemas Mecânicos*. Porto: Faculdade de Engenharia da Universidade do Porto, 2014.

[27] P. Avitabile, *Modal Testing: A Practitioner's Guide*. 2017.

[28] B. Peeters, H. Van Der Auweraer, P. Guillaume, and J. Leuridan, "The PolyMAX frequency-domain method: A new standard for modal parameter estimation?," *Shock and Vibration*, vol. 11, no. 3-4, pp. 395–409, 2004.

[29] B. Peeters, M. El-Kafafy, and P. Guillaume, "The new PolyMAX plus method: Confident modal parameter estimation even in very noisy cases," *International Conference on Noise and Vibration Engineering 2012, ISMA 2012, including USD 2012: International Conference on Uncertainty in Structure Dynamics*, vol. 4, no. January, pp. 2801–2813, 2012.

[30] R. Brincker and C. Ventura, *Introduction to Operational Modal Analysis*. John Wiley Sons, 2015.

[31] C. Rainieri and G. Fabbrocino, *Operational Modal Analysis of Civil Engineering Structures: An Introduction and Guide for Applications*. New York: Springer-Verlag, 1st ed.

[32] E. M. C. Jones, M. A. Iadicola, R. Bigger, B. Blaysat, C. Boo, M. Grewer, J. Hu, A. Jones, M. Klein, K. Raghavan, P. Reu, T. Schmidt, T. Siebert, M. Simenson, D. Turner, A. Vieira, and T. Weikert, "A Good Practices Guide for Digital Image Correlation," *International Digital Image Correlation Society*, p. 94, 2018.

[33] B. Pan, "Recent Progress in Digital Image Correlation," *Experimental Mechanics*, vol. 51, no. 7, pp. 1223–1235, 2011.

[34] M. A. Sutton, "Digital Image Correlation for Shape and Deformation Measurements," pp. 565–600.

[35] E. Di Lorenzo, D. Mastrodicasa, L. Wittevrongel, P. Lava, and B. Peeters, "Full-field modal analysis by using digital image correlation technique," *Conference Proceedings of the Society for Experimental Mechanics Series*, 2020.

[36] Y. Liu, H. Gao, J. Zhuge, and J. Zhao, "Research of under-sampling technique for digital image correlation in vibration measurement," *Conference Proceedings of the Society for Experimental Mechanics Series*, vol. 9B, pp. 49–58, 2017.

[37] S. R. Jambovane, D. J. Kalsule, and S. M. Athavale, "Validation of FE Models Using Experimental Modal Analysis," *SAE Technical Papers*, vol. 2001-January, no. January, 2001.

[38] R. J. Allemang, "The modal assurance criterion - Twenty years of use and abuse," *Sound and Vibration*, vol. 37, no. 8, pp. 14–21, 2003.

Appendix A

Modal Parameters of the Dryer Machine

Natural Frequencies									
	EMA						OMA		
Mode	Hammer			Shaker			Operational		
	ACC	DIC	Error(%)	ACC	DIC	Error(%)	ACC	DIC	Error(%)
1	21.59	21.59	0.01	21.90	21.88	0.10	21.35	20.48	4.09
2	31.81	31.73	0.25	32.45	32.37	0.23	28.99	27.56	4.94
3	37.25	37.00	0.67	37.50	37.00	1.34	37.09	36.97	0.32
4	46.40	46.96	1.20	47.64	47.87	0.49	47.66	47.87	0.45
5	52.87	53.06	0.36	-	53.17	-	-	51.87	-
6	58.32	58.11	0.37	57.28	58.34	1.84	58.47	58.97	0.85
7	-	-	-	-	63.37	-	-	-	-
8	78.89	78.21	0.86	78.15	78.54	0.50	78.92	78.00	1.17
9	91.29	92.63	1.46	-	-	-	-	92.33	-
10	98.22	98.31	0.09	98.29	98.30	0.01	99.88	98.77	1.11
11	105.63	105.43	0.20	107.49	106.73	0.71	105.50	104.99	0.48
12	117.30	117.44	0.12	117.97	117.02	0.81	116.68	116.86	0.15
13	127.09	126.48	0.49	126.55	126.49	0.05	-	126.15	-
14	135.75	135.91	0.11	135.13	135.23	0.07	135.74	135.87	0.09
15	153.08	150.49	1.69	153.02	153.10	0.05	152.86	-	-
16	161.62	163.80	1.35	160.71	160.64	0.04	161.91	-	-
17	178.34	177.31	0.58	-	177.64	-	177.55	-	-
18	186.34	186.77	0.23	186.43	185.08	0.72	186.75	-	-
19	191.21	192.25	0.55	-	190.36	-	-	-	-
20	200.55	-	-	203.41	-	-	-	-	-
21	207.45	207.24	0.10	-	205.48	-	206.30	-	-
22	222.60	224.13	0.69	-	-	-	223.84	-	-
23	231.55	232.13	0.25	-	-	-	230.78	-	-
24	237.21	-	-	-	-	-	-	-	-
25	244.82	243.76	0.43	-	243.50	-	244.60	-	-

26	250.01	-	-	-	251.44	-	-	-	-
27	264.94	264.08	0.32	266.93	-	-	265.16	-	-
28	272.08	272.03	0.02	272.82	-	-	272.34	-	-
29	-	-	-	284.73	287.19	0.87	-	-	-
30	300.18	301.31	0.38	298.85	-	-	299.20	-	-
31	314.09	316.06	0.63	314.78	311.52	1.04	314.82	-	-
32	326.73	324.54	0.67	325.87	325.84	0.01	327.02	-	-
33	-	-	-	336.01	336.37	0.11	-	-	-
34	350.83	351.93	0.31	-	-	-	-	-	-
35	357.94	-	-	358.51	361.53	0.84	356.76	-	-
36	371.76	-	-	-	371.52	-	370.61	-	-
37	382.85	-	-	-	-	-	-	-	-
38	387.94	-	-	387.04	389.19	0.55	387.61	-	-
39	395.37	-	-	398.31	397.76	0.14	399.22	-	-
40	-	-	-	-	-	-	412.76	-	-
41	-	-	-	421.84	421.45	0.09	427.39	-	-
42	-	-	-	434.73	436.95	0.51	-	-	-
43	-	-	-	472.81	472.58	0.05	-	-	-
44	-	-	-	-	-	-	480.92	-	-
45	-	-	-	-	-	-	554.38	-	-
46	-	-	-	-	-	-	579.27	-	-
47	-	-	-	-	-	-	589.63	-	-
48	-	-	-	-	-	-	651.37	-	-
49	-	-	-	-	-	-	671.52	-	-
50	-	-	-	-	-	-	694.93	-	-
51	-	-	-	-	-	-	735.90	-	-
52	-	-	-	-	-	-	772.80	-	-

Damping Ratios									
	EMA						OMA		
Mode	Hammer			Shaker			Operational		
	ACC	DIC	Error(%)	ACC	DIC	Error(%)	ACC	DIC	Error(%)
1	3.14	2.56	18.36	2.10	2.10	0.20	3.39	3.81	12.59
2	3.23	3.09	4.62	1.25	2.88	129.98	9.27	5.95	35.77
3	0.51	0.68	33.70	0.38	1.37	260.25	6.91	1.32	80.91
4	1.54	2.39	55.38	1.84	3.15	70.88	0.53	1.35	155.47
5	0.62	0.97	56.18	-	2.54	-	-	0.88	-
6	1.16	1.70	47.07	0.40	0.96	140.62	0.65	0.76	16.47
7	-	-	-	-	1.68	-	-	-	-
8	0.62	0.46	26.14	0.55	0.88	59.57	0.69	0.99	43.95
9	3.65	1.24	66.15	-	-	-	-	0.74	-
10	0.95	0.96	0.75	0.48	0.65	34.45	0.67	0.64	5.39
11	1.48	2.13	43.45	2.92	1.65	43.52	1.09	1.08	1.61
12	1.08	0.83	22.64	0.87	0.95	8.51	1.58	0.56	64.41
13	0.46	0.55	19.62	0.53	0.66	25.21	-	0.55	-
14	0.51	0.69	33.67	0.50	0.74	48.42	0.62	0.56	10.12
15	0.84	0.65	22.89	1.37	0.81	41.44	0.72	-	-
16	0.34	1.82	443.06	1.02	0.54	46.62	0.35	-	-
17	0.55	0.28	47.98	-	1.08	-	0.94	-	-
18	0.89	1.04	16.49	2.86	0.33	88.35	0.37	-	-
19	0.60	0.93	54.87	-	0.42	-	-	-	-
20	0.95	-	-	2.81	-	-	-	-	-
21	0.60	0.80	31.95	-	0.80	-	0.66	-	-
22	1.18	1.18	0.20	-	-	-	0.97	-	-
23	1.15	1.34	16.34	-	-	-	1.64	-	-
24	1.15	-	-	-	-	-	-	-	-
25	0.94	1.67	77.95	-	0.38	-	1.11	-	-
26	0.81	-	-	-	0.52	-	-	-	-
27	1.97	2.30	17.21	1.00	-	-	1.27	-	-
28	0.29	0.72	147.13	0.71	-	-	0.39	-	-
29	-	-	-	0.98	0.57	41.47	-	-	-
30	0.72	1.10	53.37	0.33	-	-	0.73	-	-
31	0.92	0.92	0.12	1.46	0.78	46.89	1.07	-	-
32	1.50	0.04	97.50	1.39	0.26	81.00	1.01	-	-
33	-	-	-	0.63	7.07	1022.18	-	-	-
34	0.79	0.03	96.15	-	-	-	-	-	-
35	0.89	-	-	2.38	0.24	90.14	1.12	-	-
36	0.97	-	-	-	1.05	-	0.82	-	-
37	0.39	-	-	-	-	-	-	-	-
38	0.86	-	-	1.56	0.35	77.38	0.71	-	-
39	1.03	-	-	1.47	0.50	66.17	0.81	-	-
40	-	-	-	-	-	-	0.60	-	-

41	-	-	-	0.87	2.09	141.18	1.25	-	-
42	-	-	-	0.98	0.15	84.93	-	-	-
43	-	-	-	1.58	0.23	85.36	-	-	-
44	-	-	-	-	-	-	1.29	-	-
45	-	-	-	-	-	-	0.77	-	-
46	-	-	-	-	-	-	0.53	-	-
47	-	-	-	-	-	-	0.49	-	-
48	-	-	-	-	-	-	0.23	-	-
49	-	-	-	-	-	-	0.54	-	-
50	-	-	-	-	-	-	0.66	-	-
51	-	-	-	-	-	-	0.46	-	-
52	-	-	-	-	-	-	0.25	-	-